A 6-DOF sliding mode fault tolerant control solution for in-orbit autonomous rendezvous

David Henry, Jazmin Zenteno-Torres, Jérôme Cieslak, Alejandra Ferreira de Loza, Jorge Dávila

Version of Record: https://www.sciencedirect.com/science/article/pii/S1270963821005605
Manuscript_719fd6586b2149869dc8c491542209af

A 6-DOF Sliding Mode Fault Tolerant Control Solution for In-Orbit Autonomous Rendezvous

David Henry[a,d], Jazmin Zenteno-Torres[a], Jérôme Cieslak[a], Alejandra Ferreira De Loza[b], Jorge Dávila[c]

[a] *IMS lab., Univ. Bordeaux, Bordeaux INP, CNRS (UMR 5218), 351 Cours de la libération, 33405, Talence, France*
[b] *Cátedras CONACyT at Instituto Politécnico Nacional, CITEDI, Avenida del Parque 1310, Mesa de Otay, Tijuana, 22510, México*
[c] *Instituto Politécnico Nacional IPN, Section of Graduate Studies and Research ESIME-UPT, Av. Ticomán 600, San José Ticomán, C.P.07340, México*
[d] *Corresponding author*

Abstract

The goal pursued by this article, is to evaluate the potential of sliding-mode control and estimation techniques, to address fault tolerance against a large class of actuator faults, including loss of controllability of the faulty actuator, for autonomous rendezvous between a chaser spacecraft and a passive spacecraft on a circular orbit. The proposed solution is based on the dual quaternion formalism, to describe in a single equation, rotational and translational spacecraft dynamics, solar array flexible modes, propellant sloshing, the most dimensioning space disturbances, and their coupling. Such a modelling formalism enables to propose a six degree-of-freedom fault tolerant control architecture, which relies on the generalized super-twisting control algorithm nested with a nonlinear fault estimator. An anti-windup strategy based on polytope algebra is applied to the control algorithm, to prevent instability due to actuator saturation when faults occur. Asymptotic stability of the proposed fault-tolerant control scheme is formally proved with respect to a wide variety of faults, providing that the first derivatives of the fault estimation error versus time and the sliding surface, are bounded. Intensive simulations from a functional engineering simulator that accurately simulates the rendezvous mission, are presented in the paper, as well as capture-oriented criteria. The presented results demonstrate that the proposed fault-tolerant solution is able to cover any kind of thruster faults, including total loss of controllability of the faulty thruster, as well as solar array flexible modes, propellant sloshing, gravity gradient, the second zonal harmonic, atmospheric drag and magnetic disturbances.

Keywords: Fault-tolerant control, sliding mode control, generalized super twisting algorithm, dual quaternion, in-orbit autonomous rendezvous.

1. Introduction and Motivations

Development of autonomous strategies for the final approaching phase of an on-orbit rendezvous between two spacecraft, is a key technology. In this phase, the chaser approaches the target along a straight line as much as possible, in order to satisfy the strict requirements of docking for the relative position, velocity, attitude, and angular rate. A trajectory-attitude combined control strategy of six-degrees of freedom (6-DOF) approaches, is usually used for that purpose [73, 69, 3, 90, 42, 24, 96, 54, 9, 26, 8, 7, 10, 76]. Different model formalisms can be used to design a 6-DOF rendezvous controller. One can cite the Cartesian coordinates and Euler angles [87, 60], the quaternions [51, 59], the modified Rodrigues parameters [77], the special Euclidean group [53] and the dual-quaternions (DQs) [50, 85, 16]. A great advantage of DQ's formalism, is that it describes the rotational and translational dynamics in a single equation, instead of defining separate equations. DQs offer a singularity-free, compact and unambiguous form for representing transforms. Thus, DQs cut down the volume of algebra [50]. This motivated its application in different fields like image processing [82], robotics [12], navigation [88], computer graphics [49] and control [20, 83, 85], to mention some.

In this paper, the DQ's formalism is used to develop a DQ–based Fault-Tolerant Control (FTC) scheme, able to cover a large class of faults occurring in the thruster-based propulsion unit of a spacecraft. The solution belongs to the class of Sliding-Mode Control (SMC) approaches. More precisely, the FTC solution relies on the Generalized Super Twisting Algorithm (GSTA) [61, 4], which is nested by a nonlinear fault estimator and an original anti-windup strategy. The reference scenario consists of a chaser's spacecraft performing a rendezvous with a passive spacecraft, on a circular orbit around Earth.

There exist plenty of FTC solutions developed by the academic community that can be applied to in-orbit autonomous rendezvous missions, see the recent books [78, 14, 64, 43]. Active FTC solutions are characterized by the use of fault information

Email addresses: david.henry@ims-bordeaux.fr (David Henry), jazmin.zenteno-torres@ims-bordeaux.fr (Jazmin Zenteno-Torres), jerome.cieslak@ims-bordeaux.fr (Jérôme Cieslak), dferreira@citedi.mx (Alejandra Ferreira De Loza), jadavila@ipn.mx (Jorge Dávila)

provided by a fault diagnosis unit, and control redesign based on this information. Fault information can be obtained from the procedures of fault detection and fault isolation (FDI). Many FDI methods are based on residual generator designs, see the books [63, 13, 81]. The principle consists of a set of residuals whose structure, time and frequency behaviour are analysed to determine fault location, magnitude and time occurrence. Generally speaking, FDI schemes are based on many dynamic filters and thus lead to some complex FDI schemes, as opposed to fault estimation (FE) that directly reconstructs the fault shape [64]. Furthermore, it is straightforward to note that the FE signals are conveniently available for use in a scheme, to robustly compensate the fault effects within control loops. This technique is referred as the FE–based FTC technique and it can be noted that attention has recently been paid on adaptive [70] and sliding mode [91] approaches. The reason seems quite evident: These paradigms offer solutions to both robust fault estimation and robust control. The FTC technique that is proposed in this paper belongs to the sliding-mode FE–based FTC category.

It is worth noting that there is no proof of any separation principle in many proposed FE–based FTC techniques. Thus, the coupling between the fault reconstruction and the control units, is rarely investigated. Furthermore, putting the FE unit and the controller together, does not guarantee that the overall FTC solution is globally optimal, even if they are tuned optimally separately. A solution to these problems is studied in [52, 64] by using adaptive gain for the observer and the adaptive backstepping control technique. This problem is too addressed in [18, 5] with FDI procedures, using the switching control theory. In this paper, asymptotic stability is formally proved within the sliding-mode framework, providing that the first derivatives of the FE error versus time and the sliding surface, are bounded.

Coming back to sliding mode FE–based FTC solutions and focussing especially on space applications, one can mention the works reported in [32, 48, 95] for spacecraft attitude tracking subject to actuator faults. Fault tolerance against actuator faults is ensured using adaptive nonsingular Terminal Sliding Mode (TSM) control technique. A finite-time extended state observer that estimates the faults, is integrated into a fast nonsingular TSM controller in [56], and in [55] using the supertwisting algorithm, to provide a continuous attitude FTC algorithm. Fixed-time sliding mode control is proposed in [45] for attitude control under actuator saturation and faults. The work reported in [46] develops a FTC scheme for rendezvous and docking with a freely tumbling target in the presence of thruster loss-of-efficiency fault types. In [25], the proposed solution is based on the backstepping control and integral SMC technique. The control law is also nested by an adaptive nonlinear fault estimation observer, which is in charge to estimate the value of unknown time-varying faults. The principle of integral SMC is too proposed in [71]. It is shown that the closed-loop system is capable of tolerating actuator faults, by means of one-parameter dependent adaptive mechanism. A fast TSM control approach is proposed in [72]. The solution not only has the capability to protect the actuator from saturation but also guarantees that attitude and angular velocity converge to a neighbourhood of the origin in finite time. The authors in [27] develop a nonsingular fixed-time terminal SMC scheme. In this work, the FTC problem is formulated as a prescribed performance control problem. It is proved that the attitude of the spacecraft is kept within the predefined constraint boundaries, even when the actuator saturation is taken into account. An anti-unwinding finite time fault tolerant sliding mode control solution is also considered in [68]. The solution reported in [23] considers the attitude's FTC problem under uncertainties and control saturation, by means of a fast nonsingular terminal SMC technique and fuzzy logic rules. As opposed to [57, 58], the proposed solution can handle actuator failures and saturations in a less conservative manner, following the authors' opinion. In [66] fuzzy logic rules are used, to estimate (approximate to be more precise) the faults. The estimates are re-injected into a fractional-order SMC law that uses a double power exponential reaching law and the backstepping control approach. In a very similar fashion, neural network and adaptive first-order SMC are used in [89]. The proposed solution also protects the control law from actuator position saturation with globally asymptotically attitude tracking. The work reported in [39] ensures fault tolerance using a nonlinear integral SMC approach. The solution consists of an adaptive fault observer and a control gain adaption method, based on dual-layer gain adaptation scheme. By combining the finite-time passivity technique into adaptive sliding mode control approach, a smooth fault-tolerant control algorithm is proposed in [41] for attitude tracking. Finally, in [29], the authors propose an integral terminal sliding-mode controller such that the sliding motion realizes the action of a quaternion-based nonlinear proportional-derivative controller. Adaptive techniques are used and the resultant adaptive SMC law stabilizes the system states to a small neighbourhood around the sliding surface, in finite time.

One can point out the following limitations from the above current practice of SMC for FTC. Many FTC solutions are concerned by the attitude control problem. So a 6-DOF structure has been rarely investigated. The case of a complete loss of actuators is not covered. Most of the studied fault profiles are restricted to smooth fault profiles, which comes from the necessity of providing smooth estimates of the fault. It is also possible to consider a discontinuous fault profile. But in this case, the use of the equivalent output injection to reconstruct the fault, will require the application of a filter, providing only an asymptotic estimation of the fault. The fault signal, and its derivatives up to a certain order for certain techniques, is always assumed to be bounded. Finally, the proposed solutions have not been evaluated under a high realistic environment. Especially, none have been evaluated, considering simultaneously the effect of the solar array flexible modes, propellant sloshing, a realistic navigation unit and the perturbing accelerations coming from the space environment. This is of prime interest when considering a 6-DOF FTC solution since these phenomena cause a coupling between translation and rotation motions. That is probably why SMC techniques have not retained attention for FTC by the space agencies and industries for real space

missions[1]. Indeed, the most popular solution is the constrained control allocation (CA) technique. This approach is studied in [22] for the Mars Sample Return mission[2] and in [7, 10, 35] for the e.Deorbit mission[3], with validation on industrial test facilities. The principle consists in scheduling the control allocation algorithm that manages the thruster command signals, so that the total forces and torques are re-allocated on the healthy thrusters. This means that the fault tolerance mechanism operates at the thruster management unit, and not really at the control level. Such a solution requires obviously a (reliable) fault diagnosis unit, so that the control allocation algorithm is aware about the faulty thrusters. The interested reader can refer to [33, 22, 37, 65, 34, 35] for the development of model-based diagnosis solutions applied to real space missions[4]. This FTC strategy is used in [15] with a time-varying terminal SMC approach and in [28] in cooperation with an adaptive integral SMC technique. However, it is worth noting that the fault diagnosis algorithm is neither developed, nor described in these papers. The CA technique is used too for actuator fault tolerance in [40]. The proposed solution relies on an iterative learning observer in charge of estimating the torque deviation, and an integral-type sliding mode control law, to produce the three-axis virtual control signals that are allocated by the CA algorithm.

This paper aims at covering most of the aforementioned limitations. Key ingredients are:

i) A 6-DOF FTC solution is proposed based on the DQ formalism, resulting in a singularity-free, compact and unambiguous FTC solution.

ii) The proposed solution is valid for non-bounded faults (including abrupt and totally uncontrollable actuators), which is rarely the case for most existing sliding-mode FTC solutions. However, it should be pointed out that the first derivatives versus time and the sliding surface of the fault estimation error, are required to be bounded, in the l_∞-norm sense.

iii) A formal proof of stability of the overall fault-tolerant scheme is provided. The proof also takes into account the coupling between the fault estimator and the controller.

iv) An anti-windup strategy based on polytope algebra is considered, to avoid instability of the FTC loop. This point becomes especially crucial when dealing with FTC problems, since abrupt faults cause actuator saturation.

v) The proposed solution is evaluated under a high-fidelity functional engineering simulator (FES) that considers the simultaneous effects of the solar array flexible modes, propellant sloshing, a realistic navigation unit, Earth gravity, J_2, atmospheric drag and magnetic disturbances.

The solution relies, *i*) on an inner control loop that is based on a nonlinear estimator in charge of estimating faults, and, *ii*) an outer control loop based on the GSTA. This solution is built upon our previous works presented in [93, 94, 80]. These papers present control solutions based on the Clohessy-Wiltshire-Hill relative position model and the Euler angles with first-order SMC [93, 94] and the super-twisting algorithm [80]. However, neither fault tolerance, nor control saturation problems and the DQ formalism, have been considered in our previous works.

The FTC solution proposed in this article uses a high-order sliding-mode algorithm as a base, leading to a system of differential equations with discontinuous right-hand side. The corresponding solutions will thus be understood in the Filippov sense [21]. Filippov solutions, which coincide with the classical solutions when the right-hand side of the differential equation is continuous, are absolutely continuous by definition (see, for example, [74] for a comprehensive tutorial on the different alternative solution notions of discontinuous dynamical systems).

The paper is organized as follows: Section 2 gives material backgrounds. Section 3 explains the considered rendezvous mission. The main disturbances and modelling considerations are presented in Section 4, and finally states the problem. Section 5 is concerned by the proposed FTC solution. Finally, section 6 is dedicated to simulation results.

2. Material background

2.1. Dual-vectors, dual-quaternions and dynamics of a rigid body

A dual-number is defined as $\bar{a} = a_r + \varepsilon a_d$ where a_r and a_d are called the real part and the dual part, respectively. ε is the so-called dual unit which is defined as $\varepsilon^2 = 0$ but $\varepsilon \neq 0$. A particular class of a dual-number is the dual-vector (DV), which is defined as $\bar{\mathbf{v}} = \mathbf{v}_r + \varepsilon \mathbf{v}_d$ with $\mathbf{v}_r$ and $\mathbf{v}_d$, the real and the dual parts of $\bar{\mathbf{v}}$ respectively, that are both real vectors. The set of DVs are denoted in this paper $\mathbb{V}$, which is defined according to $\mathbb{V} = \{\bar{\mathbf{v}} : \bar{\mathbf{v}} = \mathbf{v}_r + \varepsilon \mathbf{v}_d,\ \mathbf{v}_r, \mathbf{v}_d \in \mathbb{R}\}$. The notation $\mathbb{V}^n$ is used to refer to the set of DVs of dimension n.
Quaternions are defined as the extension of complex numbers to hypercomplex numbers [6, 30]. The set of quaternions is defined by $\mathbb{H} = \{\mathbf{q} : \mathbf{q} = (s, \boldsymbol{v})\}$ where s is a scalar and $\boldsymbol{v}$ is a vector. An alternative definition of the quaternion is $\mathbf{q} = q_0 + q_1 i + q_2 j + q_3 k,\ \ q_i \in \mathbb{R}, i = \overline{0, 3}$ so that q_0 is the scalar part and $[q_1, q_2, q_3]^T$ is the vector part, and i, j, k satisfy the following properties: $i^2 = j^2 = k^2 = -1, i = jk = -kj, j = ki = -ik$.
Based on the concepts of quaternions and DVs, a Dual Quaternion (DQ) $\bar{\mathbf{q}}$ is defined by $\bar{\mathbf{q}} = (\bar{s}, \bar{\boldsymbol{v}})$ where $\bar{s}$ is a dual scalar (i.e. a dual-vector of dimension 1) and $\bar{\boldsymbol{v}}$, a dual-vector. An alternative of the DQ's definition is $\bar{\mathbf{q}} = \mathbf{q}_r + \varepsilon \mathbf{q}_d$, so that it has, as

[1] Following the expertise of D. Henry which is an expert for CNES (French Space agency) and has many collaborations with ESA and the most famous space industries in Europe.
[2] see https://www.esa.int/Science_Exploration/Human_and_Robotic_Exploration/Exploration/Mars_sample_return
[3] see https://www.esa.int/Safety_Security/Clean_Space/ESA_s_e.Deorbit_debris_removal_mission_reborn_as_servicing_vehicle
[4] Real missions are the Microscope satellite, the Myriade platform, the Mars Sample Return and e.Deorbit missions

elements, two quaternions $\mathbf{q}_r \in \mathbb{H}$ and $\mathbf{q}_d \in \mathbb{H}$ that represent its real and dual parts, respectively. In this paper, the set of DQs is defined by $\mathbb{H}_d = \{\bar{\mathbf{q}} : \bar{\mathbf{q}} = \mathbf{q}_r + \varepsilon\mathbf{q}_d,\ \varepsilon^2 = 0, \varepsilon \neq 0,\ \mathbf{q}_r, \mathbf{q}_d \in \mathbb{H}\}$.

The formulation of rigid body dynamics in terms of DQs, has been investigated by different authors that propose diverse formalisms [17, 31, 86, 2, 84, 19, 20]. In this paper, we use the formalism proposed by [84]. It consists in describing the rotational and translational dynamics by means of the so-called "dual-inertia operator" $\bar{\boldsymbol{M}}$, defined as:

$$\bar{\boldsymbol{M}} = m\frac{d}{d\varepsilon}\mathbf{I}_3 + \varepsilon\boldsymbol{J} = \begin{bmatrix} m\frac{d}{d\varepsilon} + \varepsilon J_{xx} & \varepsilon J_{xy} & \varepsilon J_{xz} \\ \varepsilon J_{xy} & m\frac{d}{d\varepsilon} + \varepsilon J_{yy} & \varepsilon J_{yz} \\ \varepsilon J_{xz} & \varepsilon J_{yz} & m\frac{d}{d\varepsilon} + \varepsilon J_{zz} \end{bmatrix} \tag{1}$$

m is the mass of the body and $\boldsymbol{J}$ is the inertia of the body about its center-of-mass, written in the body frame. The operator $\frac{d}{d\varepsilon}$ on the dual object $\bar{a}$ is defined by $\frac{d}{d\varepsilon}\bar{a} = \frac{d}{d\varepsilon}(a_r + \varepsilon a_d) = a_d$ and $\left(\frac{d}{d\varepsilon}\right)^2 = 0$. $\mathbf{I}_3$ is the identity in dimension 3.

2.2. Used operations

Given two DVs $\bar{\mathbf{v}}_1 = \mathbf{v}_{1r} + \varepsilon\mathbf{v}_{1d}$ and $\bar{\mathbf{v}}_2 = \mathbf{v}_{2r} + \varepsilon\mathbf{v}_{2d}$ in $\mathbb{V}$, the sum, dot and cross products are defined in $\mathbb{V}$, respectively by:

$$\bar{\mathbf{v}}_1 + \bar{\mathbf{v}}_2 = \mathbf{v}_{1r} + \mathbf{v}_{2r} + \varepsilon(\mathbf{v}_{1d} + \mathbf{v}_{2d}) \tag{2}$$

$$\bar{\mathbf{v}}_1.\bar{\mathbf{v}}_2 = \mathbf{v}_{1r}.\mathbf{v}_{2r} + \varepsilon(\mathbf{v}_{1r}.\mathbf{v}_{2d} + \mathbf{v}_{1d}.\mathbf{v}_{2r}) \tag{3}$$

$$\bar{\mathbf{v}}_1 \times \bar{\mathbf{v}}_2 = \mathbf{v}_{1r} \times \mathbf{v}_{2r} + \varepsilon(\mathbf{v}_{1r} \times \mathbf{v}_{2d} + \mathbf{v}_{1d} \times \mathbf{v}_{2r}) \tag{4}$$

The conjugate of a DQ $\bar{\mathbf{q}} = (\bar{s}, \bar{\boldsymbol{v}})$ is given by $\bar{\mathbf{q}}^* = (\bar{s}, -\bar{\boldsymbol{v}})$. Given two DQs $\bar{\mathbf{q}}_1 = (\bar{s}_1, \bar{\boldsymbol{v}}_1)$ and $\bar{\mathbf{q}}_2 = (\bar{s}_2, \bar{\boldsymbol{v}}_2)$ in $\mathbb{H}_d$, we define the following operations:

$$\bar{\mathbf{q}}_1 + \bar{\mathbf{q}}_2 = (\bar{s}_1 + \bar{s}_2, \bar{\boldsymbol{v}}_1 + \bar{\boldsymbol{v}}_2) \tag{5}$$

$$\bar{\mathbf{q}}_1 \circ \bar{\mathbf{q}}_2 = (\bar{s}_1\bar{s}_2 - \bar{\boldsymbol{v}}_1.\bar{\boldsymbol{v}}_2, \bar{s}_1\bar{\boldsymbol{v}}_2 + \bar{s}_2\bar{\boldsymbol{v}}_1 + \bar{\boldsymbol{v}}_1 \times \bar{\boldsymbol{v}}_2) \tag{6}$$

The operation $\bar{\mathbf{q}} \circ \bar{\mathbf{v}}$ between a DQ and a DV of dimension 3 is defined as the operation (6), where the second DQ has its scalar part fixed to 0. Note that these operations are similar to that of the standard quaternion.
Given a DV $\bar{\mathbf{v}} \in \mathbb{V}$ and a dual inertia operator $\bar{\boldsymbol{M}}$, the product $\bar{\boldsymbol{M}}\bar{\mathbf{v}}$ is defined by [2]

$$\bar{\boldsymbol{M}}\bar{\mathbf{v}} = m\mathbf{v}_d + \varepsilon\boldsymbol{J}\mathbf{v}_r \tag{7}$$

Finally, the inverse of $\bar{\boldsymbol{M}}$ is given by [2]

$$\bar{\boldsymbol{M}}^{-1} = \boldsymbol{J}^{-1}\frac{d}{d\varepsilon} + \varepsilon\frac{1}{m}\mathbf{I}_3 \tag{8}$$

3. The reference mission and the functional engineering simulator environment

The considered rendezvous scenario is the same as the one considered in [93, 94, 80]. The major differences consist of the thruster configuration matrix that has been specially designed for fault tolerance purposes and the navigation unit that is considered with realistic characteristics. Towards this end, and in order to avoid duplicating materials presented in [93, 94, 80], the following section focuses on the main characteristics of the mission.

We consider a chaser spacecraft on which it is attached a solar array with two flexible modes, and two propellant tanks partially filled, so that the propellant sloshes during chaser's manoeuvrers. The chaser's characteristics are listed in Table 2. With regards to the target, it is supposed to be a passive object, i.e. no actuator, no sensor and no telemetry unit. For the capture mechanism, it is supposed to be a basket. The orbit's rendezvous is characterised by the orbital parameters listed in Table 1. The spacecraft trajectories and attitudes are illustrated on Fig. 2. The rendezvous scenario consists of:

- chaser's rotation around its center-of-mass (CoM) to align the capture mechanism with the target.
- chaser's translation into the direction of the target to capture it. During this phase, the attitude is controlled to keep the capture mechanism aligned with the target.

Orbital parameters:	Target	Chaser
Semimajor axis (a)	$7068km$	$7068km$
Eccentricity (e)	0	0
Inclination (i)	$0rad$	$0rad$
Longitude of the ascending node (Ω)	$0rad$	$0rad$
Argument of periapsis (ω)	$0rad$	$0rad$
True anomaly (ν: $\dot{\nu} = n$)	$\nu(0) = 1,5.10^{-5}rad$	$\nu(0) = 0rad$

Table 1: Orbit's characteristics

At the actuator level, a set of 24 thrusters of 2 N equips the chaser. We shall point out that the configuration of the thrusters has been designed specially to study fault-tolerant strategies. Particularly, thrusters are organised in eight groups of three thrusters so that the configuration provides some degrees of freedom in terms of attainable forces and torques. Fig. 1 gives the position and the direction of the thrusters on the chaser spacecraft. Such a configuration is termed "a functional redundant configuration" in space industries. From a practical viewpoint, it means that the configuration of the thrusters enables to attain the torques and forces computed by the 6-DOF controller with some uncontrollable actuators, whenever the thrust they produce when faults occur. This is a prior condition for the existence of an FTC solution at the software level. In [92], it is shown that such a property can be addressed in terms of controllability analysis, attainable forces/moments domains or reachable sets. Note that, the configuration of the thrusters is inspired by the one used in [7, 10, 35]. Additionally to functional redundancy, this configuration considers plume impingement, contamination of avionics equipment, thruster performance, minimum impulse bit effects and actuation period. At the sensor level, more precisely in terms of available outputs from the navigation unit, it is assumed that the relative position, velocity, and acceleration between the two spacecraft are available, as well as the attitude, angular rate, and angular acceleration of the chaser.

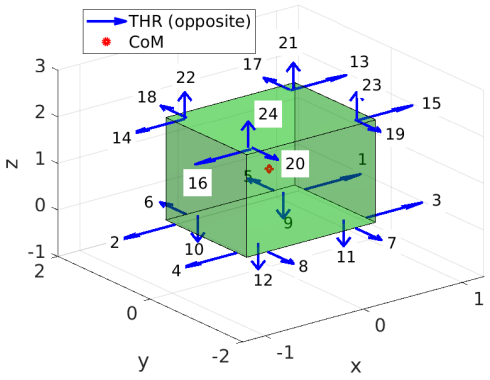

Figure 1: Thruster configuration, geometry of the chaser and CoM

The complete mission is modelled into a so-called functional engineering simulator (FES) developed in Matlab/Simulink. FES is a term used in the Space community to describe a software simulator describing at a functional level the components of a system (including its operating environment). FES is used to support the specification, design, verification and operations of space systems, and can be used across the development lifecycle, including activities such as system design validation, software verification & validation, units and sub-system test activities. The SPACELAB[5] toolbox provides the necessary set of FES's functions. It includes the ephemerides of Earth and Sun, highly representative models of sensors and actuators, and Dynamics Kinematics and Environment (DKE) models. The environment modules (within DKE) contain the environmental disturbances that may affect the rotational and translational dynamics of the spacecraft. Both spacecraft have each one an associated environment module, since the dynamics depend on specific spacecraft properties. The chaser dynamics consider the flexible modes of the solar array, the modes of the propellant sloshing and the thruster–based propulsion and sensor/navigation units. Uncertainties are included in the FES as integrated functions of the SPACELAB toolbox, such as variation of the mass, center-of-mass and inertia, uncertainties of the thruster's minimum impulse bit, thruster's misalignment and delay, thrust noise, uncertainties in the frequency modes and damping factors of the solar arrays and propellant sloshing, uncertainties in the navigation unit (caused by sensor noise and misalignment), see Table 2 for the list of considered uncertainties. In terms of environmental disturbances, the two spacecraft are assumed to be affected by the Earth gravity, the second zonal harmonic J_2, the atmospheric drag, and the magnetic disturbances.

4. Chaser and target kinematics and dynamic models

The following sections aim at establishing the models that are necessary for the derivation of the FTC solution. Such models are a key ingredient to establish a formal proof of closed-loop stability, especially under faulty conditions. Towards this end, the focus is made on establishing the DQ-based model and the FTC problem formulation. Thus, we consider neither the actuator nor the sensor and navigation models that are implemented in the FES. We argue that these models allow simulating realistic behaviours of these subsystems, e.g. thruster firing logic (firing frequency, burn resolution, minimum impulse bit), camera resolution, LIDAR noise and misalignment, etc .

4.1. Coordinate frames and notations

To establish the model of relative motion between the chaser and the target, the following coordinate frames are defined, see Fig. 2:

i) Earth-centered inertial frame $\mathcal{F}_i$: this frame is a non-accelerating reference frame, with its origin at the center of the Earth, its axis vector $\vec{x}_i$ is pointing to the vernal equinox, the axis vector $\vec{z}_i$ is pointing to the north and parallel to the rotation axis of the Earth and the axis vector $\vec{y}_i$ completes the frame.

ii) LVLH frame $\mathcal{F}_{LVLH}$: the origin of the LVLH frame is at the target CoM, its axis vector $\vec{z}_{LVLH}$ (also called "R-bar" in the rendezvous literature) is in the orbital plane, from the target's CoM towards the Earth center. Its direction vector $\vec{x}_{LVLH}$ (called "V-bar" in the rendezvous literature) is in the direction of the velocity vector of the target. Its axis vector $\vec{y}_{LVLH}$ (called "H-bar" in the rendezvous literature) is normal to the orbital plane and in the opposite direction and parallel to the orbital angular momentum vector. The LVLH frame is mainly used to plot the figures and analyse the results, since it offers a good understanding of the pose of the two spacecraft on the orbit.

iii) target frame $\mathcal{F}_t$: the center of this frame coincides with the target's CoM, and its axes are oriented in such a way that an attitude angle equal to $[0,0,0]^\intercal$ means that $\mathcal{F}_t$ coincides with $\mathcal{F}_{LVLH}$.

iv) chaser frame $\mathcal{F}_c$: the center of this frame coincides with the chaser's CoM and its axes are oriented in such a way that an attitude angle equal to $[0,0,0]^\intercal$ means that the chaser is aligned with the target along its velocity axis, so that the capture system is correctly aligned.

The notations $\boldsymbol{r}^{(i)}, \boldsymbol{r}^{(t)}, \boldsymbol{r}^{(c)}$ refer to a vector $\boldsymbol{r}$ given in the frame $\mathcal{F}_i, \mathcal{F}_t, \mathcal{F}_c$, respectively. $\boldsymbol{r}_e^{(c)}$ should be interpreted as a relative vector error between the chaser and the target, given in $\mathcal{F}_c$. Finally, $\boldsymbol{\omega}_c^{(c)}/\boldsymbol{\omega}_t^{(t)}$ denotes the angular velocity of $\mathcal{F}_c/\mathcal{F}_t$ relative to $\mathcal{F}_i$, expressed in $\mathcal{F}_c/\mathcal{F}_t$.

4.2. Dual-quaternion kinematics and dynamic models

4.2.1. The chaser case

Let $\bar{\mathbf{q}}_c \in \mathbb{H}_d$ be the DQ describing the rotation $\mathbf{q}_c \in \mathbb{H}$ of the chaser followed by a translation $\boldsymbol{r}_c \in \mathbb{R}^3$. The kinematics equation of the chaser is given by [2, 84]

$$\dot{\bar{\mathbf{q}}}_c = \frac{1}{2}\bar{\mathbf{q}}_c \circ \bar{\boldsymbol{\omega}}_c^{(c)} \tag{9}$$

[5] The SPACELAB library is a set of elementary Matlab/Simulink blocks and functions, developed by ESA (ESTEC center, Netherlands).

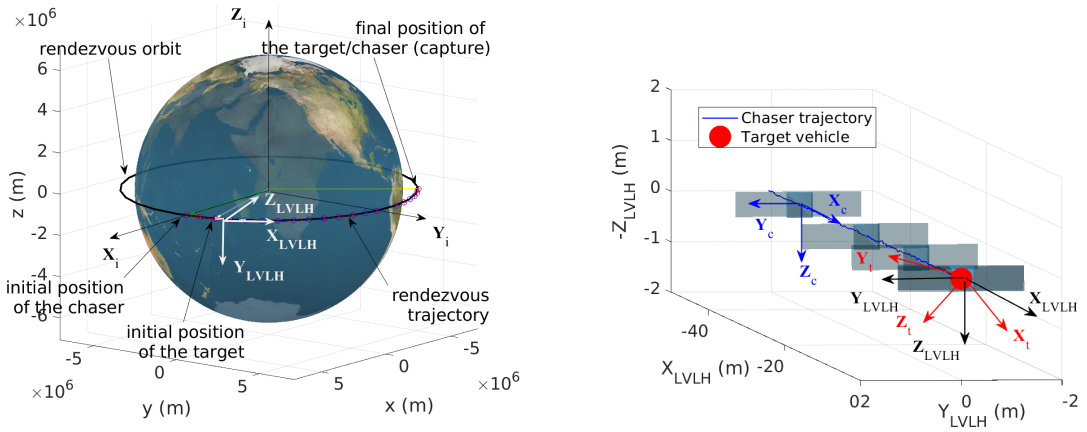

Figure 2: The orbit and rendezvous trajectory in the inertial frame (top) and in the LVLH frame, last 40m (bottom). The trajectories are built using the data presented in section 6.

where $\bar{\omega}_c^{(c)} \in \mathbb{V}^3$ is a DV, called the dual velocity of the chaser, given in the chaser frame $\mathcal{F}_c$, and defined according to:

$$\bar{\omega}_c^{(c)} = \omega_c^{(c)} + \varepsilon\left(\dot{r}_c^{(c)} + \omega_c^{(c)} \times r_c^{(c)}\right) \tag{10}$$

Consider now the dual inertia operator defined by (1), with m, the chaser's mass and $\boldsymbol{J}$, the chaser's inertia matrix about the center-of-mass, defined in the chaser frame $\mathcal{F}_c$. The dynamics equation of the chaser is given by [2, 84]

$$\dot{\bar{\omega}}_c^{(c)} = -\bar{M}^{-1}\left(\bar{\omega}_c^{(c)} \times \bar{M}\bar{\omega}_c^{(c)}\right) + \bar{M}^{-1}\bar{f}_c^{(c)} \tag{11}$$

where $\bar{f}_c^{(c)} = f_c^{(c)} + \varepsilon\tau_c^{(c)}$ is a DV in $\mathbb{V}^3$, called the total dual force applied to the center-of-mass, $f_c^{(c)} \in \mathbb{R}^3$ and $\tau_c^{(c)} \in \mathbb{R}^3$ referring to the total force and total torque, respectively.

In this work, it is considered that the total force and total torque are composed by:

- the force and the torque due to the propulsion unit, denoted $f_{c_u}^{(c)} \in \mathbb{R}^3$ and $\tau_{c_u}^{(c)} \in \mathbb{R}^3$ in the following;
- the force $f_{SA}^{(c)} \in \mathbb{R}^3$ and the torque $\tau_{SA}^{(c)} \in \mathbb{R}^3$ due to the flexible modes of the solar array;
- the force $f_P^{(c)} \in \mathbb{R}^3$ and the torque $\tau_P^{(c)} \in \mathbb{R}^3$ due to propellant sloshing;
- the Earth gravity $f_\nabla^{(c)} \in \mathbb{R}^3$;
- the force $f_{J2}^{(c)} \in \mathbb{R}^3$ due to the J_2 effect (Earth's oblateness);
- the force $f_{atm}^{(c)} \in \mathbb{R}^3$ due to atmospheric drag;
- a generalized torque disturbance $\tau_g^{(c)} \in \mathbb{R}^3$ that covers the gravity gradient, the Earth magnetic field and the atmospheric drag;
- the force $f_{c_f}^{(c)} \in \mathbb{R}^3$ and the torque $\tau_{c_f}^{(c)} \in \mathbb{R}^3$ due to the occurrence of faults in the propulsion unit.

Regarding the generalized torque disturbance $\tau_g^{(c)}$, each component is considered to be a colored noise. With regards to the Earth gravity, the atmospheric drag and the J_2 effect, they are given by [1, 44, 75] (the following equations are given in the inertial frame $\mathcal{F}_i$):

$$f_\nabla^{(i)} = -\frac{m\mu r_c^{(i)}}{\|r_c^{(i)}\|^3} \tag{12}$$

$$f_{atm}^{(i)} = -\frac{1}{2}\rho(h) S C_d \left(\dot{r}_c^{(i)}\right)^2 \tag{13}$$

$$f_{J2}^{(i)} = -\frac{3}{2}\frac{m\mu J_2 Re^2}{\|r_c^{(i)}\|^5}\left(\boldsymbol{D} - 5\left(\frac{z_c^{(i)}}{\|r_c^{(i)}\|}\right)^2 \boldsymbol{I}_3\right) r_c^{(i)} \tag{14}$$

In these equations, $S = 2\,\mathrm{m}^2$ is the dimensional cross-sectional area of the spacecraft and $C_d = 2$ is the drag coefficient. $\rho(h)$ is the atmospheric density at the altitude h. $J_2 = 0.0010826267$ and $\boldsymbol{D} = diag(1, 1, 3)$. $Re = 6378.137\,\mathrm{km}$ is the Earth's mean equatorial radius, and $r_c^{(i)} = \left[x_c^{(i)}, y_c^{(i)}, z_c^{(i)}\right]^\intercal$ is the position vector of the chaser expressed in $\mathcal{F}_i$. $\mu = 3.986\,004\,4 \times 10^{14}\,\mathrm{m}^3/\mathrm{s}^2$ is the Earth's gravitational parameter.

The flexible modes of the solar array are modelled according to [36]

$$\begin{aligned} f_{SA}^{(c)} &= -\boldsymbol{L}_f \ddot{x}_a - m_{SA}\gamma_c^{(c)}, \quad f_c^{(c)} = m\gamma_c^{(c)} \\ \tau_{SA}^{(c)} &= -\boldsymbol{L}_\tau \ddot{x}_a - \boldsymbol{J}_{SA}\dot{\omega}_c^{(c)} \end{aligned} \tag{15}$$

where $\gamma_c^{(c)}$ and $\dot{\omega}_c^{(c)}$ are derived from (11) and from the following second order vector-based equation

$$\ddot{x}_a + 2\xi\omega_0\dot{x}_a + \omega_0^2 x_a = -\boldsymbol{L}^T \begin{bmatrix} \gamma_c^{(c)} \\ \dot{\omega}_c^{(c)} \end{bmatrix} \tag{16}$$

with $x_a \in \mathbb{R}^{n_s \cdot n_p}$, $\boldsymbol{L} = [\boldsymbol{L}_f^T\ \boldsymbol{L}_\tau^T]^T, \boldsymbol{L}_f, \boldsymbol{L}_\tau \in \mathbb{R}^{3\times(n_s\cdot n_p)}$, $\boldsymbol{L}_f = \mathcal{R}(\beta)\boldsymbol{B}_T$ and $\boldsymbol{L}_\tau = \mathcal{R}(\beta)\boldsymbol{B}_R + \mathcal{S}(d)\mathcal{R}(\beta)\boldsymbol{B}_T$. n_p is the number of solar arrays and n_s is the number of flexible modes per solar array. In our application case, $n_p = 1$ and $n_s = 2$, see section

3. $\xi, \omega_0, \boldsymbol{B}_T$ and $\boldsymbol{B}_R$ refer to damping factors, frequencies and participation matrices of flexible modes. m_{SA} and $\boldsymbol{J}_{SA}$ refer to the mass and the inertia matrix of the solar array, and $\mathcal{R}(\beta)$ is a rotation matrix in charge to transform $\boldsymbol{B}_T$ and $\boldsymbol{B}_R$ given in the solar array frame, into the chaser's frame. In this work, β is considered constant since the solar array is considered to be immobile. $d \in \mathbb{R}^3$ is the distance vector between the chaser and solar array frames and $\mathcal{S}$ refers to the skew-symmetric matrix of vectors.

Propellant sloshing is modelled as a 3D-mass spring model as proposed in [36, 35], i.e.

$$\begin{aligned}
&\ddot{\boldsymbol{x}}_{s_i} + \frac{\boldsymbol{l}_{s_i}}{m_{s_i}}\dot{\boldsymbol{x}}_{s_i} + \frac{\boldsymbol{k}_{s_i}}{m_{s_i}}\boldsymbol{x}_{s_i} = \boldsymbol{\gamma}_c^{(c)}, \quad \boldsymbol{x}_{s_i} \in \mathbb{R}^3, i = 1,2 \\
&\boldsymbol{f}_P^{(c)} = (m_{s_1} + m_{s_2})\boldsymbol{\gamma}_c^{(c)} \\
&\boldsymbol{\tau}_P^{(c)} = \sum_{i=1}^{2} \boldsymbol{r}_i \times (\boldsymbol{k}_{s_i}\boldsymbol{x}_{s_i} + \boldsymbol{l}_{s_i}\dot{\boldsymbol{x}}_{s_i})
\end{aligned} \tag{17}$$

The matrices $\boldsymbol{l}_{s_i}$ and $\boldsymbol{k}_{s_i}$, $i = 1,2$ define the damping and stiffness coefficients associated to the two tanks, m_{s_i} is the propellant mass in the i-th tank and $\boldsymbol{r}_1 = \boldsymbol{r}_2$ is the distance vector between the CoM of the chaser and the CoM of the fuel in a tank.

The numerical value of the main characteristics considered in this paper are listed in Table 2. Modelling the propulsion unit and the faults are considered later, see Sections 4.4 and 4.5.

Then, using the DQ's algebra, it follows

$$\bar{\boldsymbol{f}}_c^{(c)} = \bar{\boldsymbol{f}}_{c_u}^{(c)} + \bar{\boldsymbol{f}}_{c_d}^{(c)} + \bar{\boldsymbol{f}}_{c_f}^{(c)} \tag{18}$$

where $\bar{\boldsymbol{f}}_{c_d}^{(c)} = \bar{\boldsymbol{f}}_{SA}^{(c)} + \bar{\boldsymbol{f}}_P^{(c)} + \bar{\boldsymbol{f}}_\nabla^{(c)} + \bar{\boldsymbol{f}}_{J2}^{(c)} + \bar{\boldsymbol{f}}_{atm}^{(c)} + \bar{\boldsymbol{f}}_g^{(c)}$ is the dual force about the disturbances, all terms being a DV defined in $\mathbb{V}^3$.

4.2.2. The target case

Similarly to the above developments, the kinematics and dynamic models of the target corresponds to (9),(10) and (11), where the notations "$\bullet_c$" and "$\bullet^{(c)}$" are replaced by "$\bullet_t$" and "$\bullet^{(t)}$", respectively. For instance, $\dot{\bar{\mathbf{q}}}_t = \frac{1}{2}\bar{\mathbf{q}}_t \circ \bar{\boldsymbol{\omega}}_t^{(t)}$ refers to the kinematics equation of the target. Of course, dealing with the target, the dual forces due to the actuation unit, the solar array flexible modes and propellant sloshing, do not exist, so that the total dual force that is applied to the target is concerned by the disturbances, i.e. $\bar{\boldsymbol{f}}_{t_d}^{(t)} = \bar{\boldsymbol{f}}_\nabla^{(t)} + \bar{\boldsymbol{f}}_{J_2}^{(t)} + \bar{\boldsymbol{f}}_{atm}^{(t)} + \bar{\boldsymbol{f}}_g^{(t)}$.

4.3. Dual quaternion based relative coupled dynamics

By virtue of the DQ's algebra, the motion between the target and the chaser can be expressed in the chaser frame as the relative DQ described by

$$\bar{\mathbf{q}}_e = \bar{\mathbf{q}}_t^* \circ \bar{\mathbf{q}}_c = \mathbf{q}_e + \varepsilon\frac{1}{2}\mathbf{q}_e \circ \boldsymbol{r}_e^{(c)} \tag{19}$$

where $\boldsymbol{r}_e^{(c)} = \boldsymbol{r}_c^{(c)} - \mathbf{q}_t^* \circ \mathbf{q}_c \circ \boldsymbol{r}_t^{(t)} \circ \mathbf{q}_c^* \circ \mathbf{q}_t$ is the relative position between the chaser and the target, given in the chaser frame $\mathcal{F}_c$.

Let $\bar{\boldsymbol{f}}_t^{(c)} \in \mathbb{V}^3$ be the total dual force affecting the target (see Section 4.2.2), given in the chaser frame. $\bar{\boldsymbol{f}}_t^{(c)}$ is deduced from $\bar{\boldsymbol{f}}_{t_d}^{(t)}$ by means of the following change of coordinates:

$$\bar{\boldsymbol{f}}_t^{(c)} = \bar{\mathbf{q}}_e^* \circ \bar{\boldsymbol{f}}_{t_d}^{(t)} \circ \bar{\mathbf{q}}_e \tag{20}$$

Then, and similarly to the developments presented in [2, 84], the relative kinematic and dynamic equations are given by

$$\dot{\bar{\mathbf{q}}}_e = \frac{1}{2}\bar{\mathbf{q}}_e \circ \bar{\boldsymbol{\omega}}_e^{(c)} \tag{21}$$

$$\begin{aligned}
\dot{\bar{\boldsymbol{\omega}}}_e^{(c)} = &- \bar{\boldsymbol{M}}^{-1}\left(\bar{\boldsymbol{\omega}}_c^{(c)} \times \bar{\boldsymbol{M}}\bar{\boldsymbol{\omega}}_c^{(c)}\right) + \bar{\boldsymbol{M}}^{-1}\bar{\boldsymbol{f}}_{ct}^{(c)} \\
&- \bar{\mathbf{q}}_e^* \circ \dot{\bar{\boldsymbol{\omega}}}_t^{(t)} \circ \bar{\mathbf{q}}_e + \bar{\boldsymbol{\omega}}_e^{(c)} \times (\bar{\mathbf{q}}_e^* \circ \bar{\boldsymbol{\omega}}_t^{(t)} \circ \bar{\mathbf{q}}_e)
\end{aligned} \tag{22}$$

where $\bar{\boldsymbol{f}}_{ct}^{(c)} = \bar{\boldsymbol{f}}_c^{(c)} - \bar{\boldsymbol{f}}_t^{(c)}$.

4.4. Forces and torques allocation on the thrusters

In (22), the control command is given in terms of the dual force $\bar{\boldsymbol{f}}_{c_u}^{(c)} = \boldsymbol{f}_{c_u}^{(c)} + \varepsilon\boldsymbol{\tau}_{c_u}^{(c)}$. To execute a control law practically, one need to solve the force $\boldsymbol{f}_{c_u}^{(c)}$ and torque $\boldsymbol{\tau}_{c_u}^{(c)}$ from $\bar{\boldsymbol{f}}_{c_u}^{(c)}$, and then, to allocate them on the spacecraft, by means of an actuation system. As already mentioned, we consider a set of 24 thrusters of 2 N, configured as illustrated in Fig. 1.
With this aim, equation (22) is divided into its real part and dual part. Since the capture mechanism is a simple basket, the target's rotational dynamics can be removed from (22). Then, we can derive from (22) the two following equations, that describe the rotational and translational dynamics, respectively:

$$\dot{\boldsymbol{\omega}}_e^{(c)} = -\boldsymbol{J}^{-1}\left(\boldsymbol{\omega}_e^{(c)} \times \boldsymbol{J}\boldsymbol{\omega}_e^{(c)}\right) + \boldsymbol{J}^{-1}\left(\boldsymbol{\tau}_{c_u}^{(c)} + \boldsymbol{\tau}_{ct_d}^{(c)} + \boldsymbol{\tau}_{c_f}^{(c)}\right) \tag{23}$$

$$\ddot{\boldsymbol{r}}_e^{(c)} = -\dot{\boldsymbol{\omega}}_e^{(c)} \times \dot{\boldsymbol{r}}_e^{(c)} - \boldsymbol{\omega}_e^{(c)} \times \boldsymbol{\omega}_e^{(c)} \times \boldsymbol{r}_e^{(c)} + \frac{\boldsymbol{f}_{c_u}^{(c)}}{m} + \frac{\boldsymbol{f}_{ct_d}^{(c)}}{m} + \frac{\boldsymbol{f}_{c_f}^{(c)}}{m} \tag{24}$$

In these equations, $\boldsymbol{\omega}_e^{(c)} = \boldsymbol{\omega}_c^{(c)}$, $\bar{\boldsymbol{f}}_{ct_d}^{(c)} \in \mathbb{V}^3 : \bar{\boldsymbol{f}}_{ct_d}^{(c)} = \bar{\boldsymbol{f}}_{c_d}^{(c)} - \bar{\boldsymbol{f}}_t^{(c)} = \boldsymbol{f}_{ct_d}^{(c)} + \varepsilon\boldsymbol{\tau}_{ct_d}^{(c)}$, $\boldsymbol{f}_{ct_d}^{(c)} \in \mathbb{R}^3$ and $\boldsymbol{\tau}_{ct_d}^{(c)} \in \mathbb{R}^3$ refer to the induced force and torque due to disturbances affecting both the chaser and target spacecraft, given in the chaser frame $\mathcal{F}_c$.

Remark 1. *Note that the dual quaternion–based model (21)-(22) is valid to describe the relative kinematics and dynamics (attitude and position) between two spacecraft, for any in-orbit rendezvous task. However, the separation of (22) into its real and dual parts (23) and (24), is restricted to our application case. As explained, this comes from the assumption about the particular geometry of the capture mechanism, i.e. it is assumed to be a simple basket. This is a completely different situation if the capture is made using, e.g. a robotic arm or a solid contact between a capture probe and a berthing fixture mechanism. For such capture systems, the chaser's attitude must be synchronized with the target's one to keep, e.g. the capture point attainable from the robotic end-effector or the capture probe aligned with the berthing fixture mechanism. So the target's rotational dynamics play an important role in these cases and Eqs. (23)- (24) are not valid. The authors in [84] address this issue. The result is extra terms in (23)-(24).*

Subsystem	Parameters and numerical values
MCI	Mass: $m = 300\,\text{kg}\pm1\%$ Inertia: $\boldsymbol{J} = \begin{bmatrix} 30 & 1 & 1 \\ 1 & 40 & 1 \\ 1 & 1 & 15 \end{bmatrix} \text{kg m}^2\pm10\%$ CoM (center-of-mass): [1.5 0.2 0.15]m±20%
Tank 1	Damping coeff: 0.1 ±25% Frequency of mode 1: 0.4 rad/s±2% Frequency of mode 2: 0.8 rad/s±2% Frequency of mode 3: 1 rad/s±2% Propellant mass: 10 kg
Tank 2	Damping coeff: 0.1 ±25% Frequency of mode 1: 0.4 rad/s±2% Frequency of mode 2: 0.8 rad/s±2% Frequency of mode 3: 1 rad/s±2% Propellant mass: 20 kg±2%
Solar array	Damping coeff: 3e-3 ±25% Frequency of mode 1: 0.1 rad/s±2% Frequency of mode 2: 0.5 rad/s±2% Inertia: $\boldsymbol{J}_{SA}$ =diag(10, 1, 10)kg m^2±10% Mass: $m_{SA} = 40\,\text{kg}\pm1\%$ ΔCoM chaser - SA: d = [0 2 0]m±2% Appendage angle: $\beta = 0°$ Rotation participation factor : $\boldsymbol{B}_R$: $\begin{bmatrix} 36.64 & 0 \\ 0 & 0.06 \\ 0 & -37 \end{bmatrix}$ ±20% Translation participation factor : $\boldsymbol{B}_T$: $\begin{bmatrix} 0 & 6.8 \\ -0.01 & 0 \\ 6.54 & 0 \end{bmatrix}$ ±20%

Table 2: Numerical value of the main characteristics of the chaser spacecraft (derived from the Microscope satellite [33], and the spacecraft involved in the ESA's Mars Sample Return [37, 34] and e.Deorbit [7, 10, 35] missions.)

Let $\boldsymbol{u}_c^{(c)}$ be the thruster's firing command signal vector, and $\boldsymbol{R}$ the thruster configuration matrix. Then

$$\begin{bmatrix} \boldsymbol{\tau}_{c_u}^{(c)} \\ \boldsymbol{f}_{c_u}^{(c)} \end{bmatrix} = \begin{bmatrix} \boldsymbol{R}_\tau \\ \boldsymbol{R}_f \end{bmatrix} \boldsymbol{u}_c^{(c)} = \boldsymbol{R}\boldsymbol{u}_c^{(c)}, \quad \boldsymbol{R} \in \mathbb{R}^{6\times24} \tag{25}$$

Reversing (25) is known as a Control Allocation (CA) problem. It consists in solving the following optimisation problem

$$\boldsymbol{u}_c^{(c)} = \underset{0\le u_{c_k}^{(c)} \le u_{max_k},\, k=\overline{1,24}}{argmin} \left\| \boldsymbol{W}_v \left(\boldsymbol{R}\boldsymbol{u}_c^{(c)} - \boldsymbol{v}_r \right) \right\|_p \tag{26}$$

where $\boldsymbol{v}_r$ is the vector of the desired force and torque commands and u_{max_k} is the maximum opening valve value of the k-th thruster. Here, it is equal to $u_{max_k} = 2\,\text{N}$ with $k = \overline{1,24}$. The nonsingular weighting matrix $\boldsymbol{W}_v$ affects the prioritization among force/torque components. The different choice of the vector p-norm results in minimum flow rate allocation for $p = 1$, minimum power allocation for $p = 2$ and minimum peak torque/force allocation for $p = \infty$. Any algorithm that solves the optimisation problem stated by (26) is called a CA unit, known too as a thruster management unit. Fig. 4.5 illustrates the placement of the CA unit in the control's architecture proposed in this paper. In this article, the nonlinear pseudo-inverse controller technique [47] with $p = \infty$, is used as the CA unit.

4.5. Fault-tolerant control problem formulation

With regards to the faults, since they operate at the thruster firing level, we consider the following generic fault model

$$\begin{bmatrix} \boldsymbol{\tau}_{c_u}^{(c)} \\ \boldsymbol{f}_{c_u}^{(c)} \end{bmatrix} = \boldsymbol{R}\boldsymbol{u}_c^{(c)}(t) + \boldsymbol{R}\boldsymbol{f} \quad \boldsymbol{f} \in \mathbb{R}^{24} \tag{27}$$

where $\boldsymbol{f}$ is the fault vector. Note that $\boldsymbol{f}$ is assumed to be unknown and not necessarily bounded. Thus, the faulty dual force $\bar{\boldsymbol{f}}_{c_f}^{(c)}$ is defined as

$$\bar{\boldsymbol{f}}_{c_f}^{(c)} = \boldsymbol{f}_{c_f}^{(c)} + \varepsilon\boldsymbol{\tau}_{c_f}^{(c)}, \quad \begin{bmatrix} \boldsymbol{\tau}_{c_f}^{(c)} \\ \boldsymbol{f}_{c_f}^{(c)} \end{bmatrix} = \boldsymbol{R}\boldsymbol{f} = \sum_{i=1}^{24} [...R_i...]\, f_i \tag{28}$$

This equation highlights how the faults are correlated to the torques and forces through the columns of the thruster configuration matrix $\boldsymbol{R}$. So, $R_k f_k$ is nothing else than the *kth* fault signature on the torques and forces. The indices $i = \overline{1,24}$ coincide with the numbering of thrusters as given in Fig. 1, and thus with the columns of the matrix $\boldsymbol{R}$.

$\boldsymbol{f} = 0$ means that no fault occurs in the thrusters. If the *kth* component of $\boldsymbol{f}$ is a sinus of magnitude a_0 and frequency φ_O, then the torque and the force delivered by the thrusters are modified according to

$$\begin{aligned} \boldsymbol{\tau}_{c_u}^{(c)}(t) &= \boldsymbol{R}_\tau \boldsymbol{u}_c^{(c)}(t) + R_{\tau,k} a_0 \sin(\varphi_0 t) \\ \boldsymbol{f}_{c_u}^{(c)}(t) &= \boldsymbol{R}_f \boldsymbol{u}_c^{(c)}(t) + R_{f,k} a_0 \sin(\varphi_0 t) \end{aligned} \tag{29}$$

where k refers to the *kth* thruster. Loss-of-effectiveness of the *kth* thruster can easily be considered by setting $f_k(t) = -\alpha u_{c_k}^{(c)}(t)$, with $0 < \alpha < 1$. More generally, any time function for $f_k(t)$ is suitable, including non bounded functions. However, practically the thruster's firing is limited to 2 N in our application case, so $\boldsymbol{f}(t)$ must be fixed in accordance with the saturation levels of the thrusters. Thus, with the adequate definition for $\boldsymbol{f}$, one can cover a very large class of fault profile. In particular, $\boldsymbol{f}$ can take the following form [33],

$$\boldsymbol{f}(t) = -\Psi \boldsymbol{u}_c^{(c)}(t) \tag{30}$$

with $\Psi(t) = diag\,(\psi_1(t), ..., \psi_{24}(t))$, where $0 < \psi_k(t) \le 1, k = \overline{1,24}$ are unknown. By using such a definition for $\boldsymbol{f}$, it can be observed that $\psi_k(t) = 1 - \phi_k(t)/u_{c,k}^{(c)}(t)$ with any time-dependent function $\phi_k(t)$, leads $\phi_k(t)$ to substitute the *kth* component of the control signal. Thus, the *kth* thruster's firing is exclusively driven by $\phi_k(t)$, whenever the *kth* thruster's control signal. As a consequence, with $\phi_k(t)$ defined as illustrated on Fig. 3, one can model stuck-open faults (Fig. 3 left) and stuck-closed faults (Fig. 3 right). Such faults correspond to a thruster normally operating and, suddenly goes into its maximum firing (stuck-open) or goes to a null firing (stuck-closed), at a given rate. Such faulty cases correspond to the *kth* thruster being totally

uncontrollable.

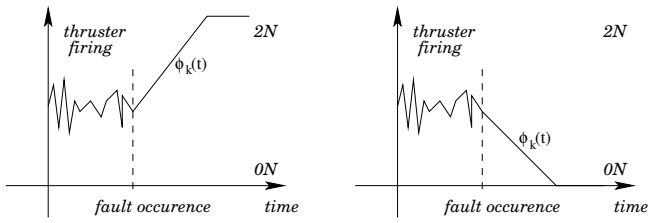

Figure 3: Stuck-open (left) and stuck-closed (right) fault profiles

Note that the formulation (27) covers both additive and multiplicative faults. If $\boldsymbol{f}$ in (27) is considered exogenous as in (29), then we face additive faults. But, if $\boldsymbol{f}$ takes the form of (30), then $\boldsymbol{f}$ is endogenous and we face multiplicative faults. With the adequate parametrization, the proposed fault model allows to cover the known on-orbit failures occurred in the missions listed in Table 3.

Spacecraft	*Cause of the fault*
Lewis	Excessive thruster firings [62]
Iridium 27	Thruster anomaly depleted operational fuel [67]
Nozomi	Thruster valve was stuck partially open [67]
Galaxy 8i	Three of four xenon ion thrusters failed [67]
EchoStar VI	Propellant leak in a thruster [79]
JCSat-1B	Thruster anomaly [11]
Myriade	Occurrences of bubbles [65]

Table 3: List of some know on-orbit failures in the thrusters

The control architecture illustrated on Fig. 4.5 is proposed to solve the FTC problem. It consists of a control signal defined by:

$$\bar{\boldsymbol{f}}^{(c)}_{FTC} = \bar{\boldsymbol{f}}^{(c)}_{sm} - \bar{\hat{\boldsymbol{f}}}^{(c)} = \boldsymbol{f}^{(c)}_{sm} - \hat{\boldsymbol{f}}^{(c)} + \varepsilon\left(\boldsymbol{\tau}^{(c)}_{sm} - \hat{\boldsymbol{\tau}}^{(c)}\right) \tag{31}$$

$\boldsymbol{f}^{(c)}_{sm}$ and $\boldsymbol{\tau}^{(c)}_{sm}$ are achieved by means of the generalized super twisting algorithm (GSTA) [61, 4]. $\hat{\boldsymbol{f}}^{(c)}$ and $\hat{\boldsymbol{\tau}}^{(c)}$ are achieved using a nonlinear estimator. It provides the estimates of the real and the dual parts of the disturbances $\bar{\boldsymbol{f}}^{(c)}_{ct_d}$ and faults $\bar{\boldsymbol{f}}^{(c)}_{c_f}$. Finally, since it is of prime importance to consider physical limitations of the thrusters, an anti-windup system is joint to the GSTA-based controller. The external anti-windup principle [38] is used here.

5. Design of the FTC system

The design of the FTC unit turns out to be the design of the disturbance/fault estimator and the GSTA control law, so that the chaser tracks an attitude and a relative position reference trajectory $(\mathbf{q}_{ref}(t), \boldsymbol{r}^{(c)}_{ref}(t))$, despite the presence of the disturbances $\bar{\boldsymbol{f}}^{(c)}_{ct_d}$ and the occurrence of faults $\bar{\boldsymbol{f}}^{(c)}_{c_f}$. Furthermore, stability must be ensured in case of thruster saturations. This is now addressed in the following sequels.

5.1. The nonlinear fault/disturbance estimator

Following equations (23) and (24), it is required to design two estimators. The first one operates at the torque level and is in charge to estimate the disturbance and fault terms $\boldsymbol{\tau}^{(c)}_{ct_d}$ and $\boldsymbol{\tau}^{(c)}_{c_f}$. The second one operates at the force level and is in charge to estimate the disturbance and fault terms $\boldsymbol{f}^{(c)}_{ct_d}$ and $\boldsymbol{f}^{(c)}_{c_f}$.

From (23), the following estimate is proposed:

$$\begin{aligned} \hat{\dot{\boldsymbol{\omega}}}^{(c)}_c &= \boldsymbol{F}_\tau + \boldsymbol{J}^{-1}\boldsymbol{\tau}^{(c)}_{c_u} \\ \boldsymbol{F}_\tau &= -\boldsymbol{J}^{-1}\left(\boldsymbol{\omega}^{(c)}_c \times \boldsymbol{J}\boldsymbol{\omega}^{(c)}_c\right) \end{aligned} \tag{32}$$

Then, it is immediate to see that

$$\dot{\boldsymbol{\omega}}^{(c)}_c - \hat{\dot{\boldsymbol{\omega}}}^{(c)}_c = \boldsymbol{J}^{-1}\left(\boldsymbol{\tau}^{(c)}_{ct_d} + \boldsymbol{\tau}^{(c)}_{c_f}\right) \tag{33}$$

and thus, that an estimate of the disturbances and fault torques (sum of the two terms $\boldsymbol{\tau}^{(c)}_{ct_d}$ and $\boldsymbol{\tau}^{(c)}_{c_f}$) can be derived directly from (33).

Similarly, the following estimate can be derived from (24)

$$\begin{aligned} \hat{\ddot{\boldsymbol{r}}}^{(c)}_e &= \boldsymbol{F}_f + \frac{\boldsymbol{f}^{(c)}_{c_u}}{m} \\ \boldsymbol{F}_f &= -\boldsymbol{\omega}^{(c)}_c \times \dot{\boldsymbol{r}}^{(c)}_e - \boldsymbol{\omega}^{(c)}_c \times \boldsymbol{\omega}^{(c)}_c \times \boldsymbol{r}^{(c)}_e \end{aligned} \tag{34}$$

An estimate of the disturbances and fault forces (sum of the two terms $\boldsymbol{f}^{(c)}_{ct_d}$ and $\boldsymbol{f}^{(c)}_{c_f}$) can be derived directly from the following equation:

$$\ddot{\boldsymbol{r}}^{(c)}_e - \hat{\ddot{\boldsymbol{r}}}^{(c)}_e = \frac{\boldsymbol{f}^{(c)}_{ct_d}}{m} + \frac{\boldsymbol{f}^{(c)}_{c_f}}{m} \tag{35}$$

We recall that the navigation unit is assumed to provide $\dot{\boldsymbol{\omega}}^{(c)}_c$, $\ddot{\boldsymbol{r}}^{(c)}_e$ and all variables that enter in $\boldsymbol{F}_\tau$ and $\boldsymbol{F}_f$, leading the aforementioned estimators, to be computationally viable.

5.2. The generalized super twisting algorithm-based controller

It is reasonable to consider that (33) and (35) provide corrupted estimates for $\boldsymbol{\tau}^{(c)}_{ct_d} + \boldsymbol{\tau}^{(c)}_{c_f}$ and $\boldsymbol{f}^{(c)}_{ct_d} + \boldsymbol{f}^{(c)}_{c_f}$. Let us denote $\boldsymbol{\tau}_\Delta$ and $\boldsymbol{f}_\Delta$ these corruption terms. It follows

$$\hat{\boldsymbol{\tau}}^{(c)} = \boldsymbol{J}\left(\dot{\boldsymbol{\omega}}^{(c)}_c - \hat{\dot{\boldsymbol{\omega}}}^{(c)}_c\right) = \boldsymbol{\tau}^{(c)}_{ct_d} + \boldsymbol{\tau}^{(c)}_{c_f} - \boldsymbol{\tau}_\Delta \tag{36}$$

$$\hat{\boldsymbol{f}}^{(c)} = m\left(\ddot{\boldsymbol{r}}^{(c)}_e - \hat{\ddot{\boldsymbol{r}}}^{(c)}_e\right) = \boldsymbol{f}^{(c)}_{ct_d} + \boldsymbol{f}^{(c)}_{c_f} - \boldsymbol{f}_\Delta \tag{37}$$

We recall that $\boldsymbol{\tau}^{(c)}_{ct_d}$ and $\boldsymbol{f}^{(c)}_{ct_d}$ include the dynamics of the flexible appendage and propellant sloshing. Then they are functions of the system's state, see Section 4.2.1. Thus, it is assumed that $\boldsymbol{\tau}_\Delta$ and $\boldsymbol{f}_\Delta$ depend too, on the system's state.

The following assumption, which guarantees that the forces and torques computed by the FTC is allocated by the CA unit on the thrusters, in the l_∞-norm sense, is now considered without loss of generality.

Assumption 2. $\left\| \left[\boldsymbol{f}^{(c)^T}_{FTC} \;\; \boldsymbol{\tau}^{(c)^T}_{FTC} \right]^T - \left[\boldsymbol{f}^{(c)^T}_{cu} \;\; \boldsymbol{\tau}^{(c)^T}_{cu} \right]^T \right\|_\infty \leq \epsilon \; with \; \epsilon \to 0.$

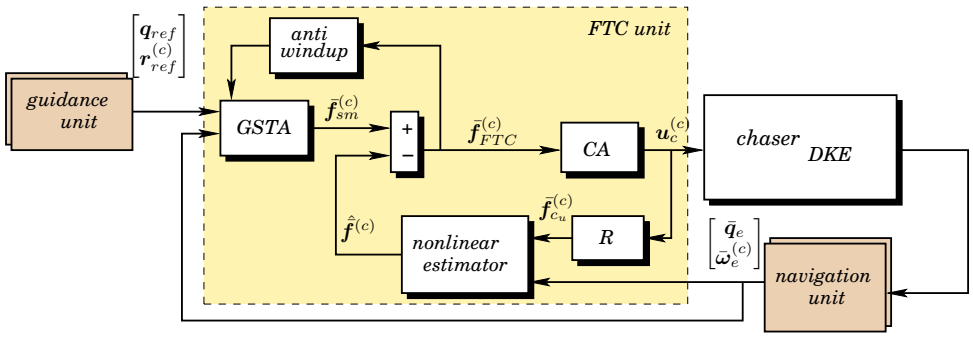

Figure 4: The chaser's GNC setup with implementation of the FTC unit at the control level. CA stands for Control Allocation, GSTA for Generalized Super Twisting Algorithm and DKE for Dynamics Kinematics and Environment

This property directly follows from the CA's characteristics described in Section 4.4. Then, with (31), (36), (37) and under assumption 2, it can be verified that (23) and (24) can be rewritten:

$$\dot{\boldsymbol{\omega}}_c^{(c)} = \boldsymbol{F}_\tau + \boldsymbol{J}^{-1}\left(\boldsymbol{\tau}_{sm}^{(c)} + \boldsymbol{\tau}_\Delta\right) \tag{38}$$

$$\ddot{\boldsymbol{r}}_e^{(c)} = \boldsymbol{F}_f + \frac{1}{m}\left(\boldsymbol{f}_{sm}^{(c)} + \boldsymbol{f}_\Delta\right) \tag{39}$$

These equations are nothing else than the dynamics to be controlled by the GSTA controller.

The following GSTA is proposed:

$$\begin{aligned}\boldsymbol{\tau}_{sm}^{(c)} =& \boldsymbol{J}\left(-\boldsymbol{F}_\tau - \boldsymbol{K}_\tau\left[\frac{1}{2}\left[(\mathbf{q}_\epsilon)_s\boldsymbol{\omega}_c^{(c)} + (\mathbf{q}_\epsilon)_v \times \boldsymbol{\omega}_c^{(c)}\right]\right]\right.\\ &\left. -\boldsymbol{\alpha}_{1\tau}\boldsymbol{\phi}_{1\tau}(\boldsymbol{s}_\tau) - \boldsymbol{\alpha}_{2\tau}\int_0^t \boldsymbol{\phi}_{2\tau}(\boldsymbol{s}_\tau(\chi))d\chi\right)\end{aligned} \tag{40}$$

$$\boldsymbol{f}_{sm}^{(c)} = m\left(-\boldsymbol{F}_f - \boldsymbol{K}_f\dot{\boldsymbol{r}}_\epsilon^{(c)} - \boldsymbol{\alpha}_{1f}\boldsymbol{\phi}_{1f}(\boldsymbol{s}_f) - \boldsymbol{\alpha}_{2f}\int_0^t \boldsymbol{\phi}_{2f}(\boldsymbol{s}_f(\chi))d\chi\right) \tag{41}$$

In these equations, $\mathbf{q}_\epsilon = \mathbf{q}_{ref}^* \circ \mathbf{q}_c$ and $\boldsymbol{r}_\epsilon^{(c)} = \boldsymbol{r}_{ref}^{(c)} - \boldsymbol{r}_e^{(c)}$ denote the chaser's quaternion tracking error and the relative position tracking error, respectively. $(\mathbf{q}_\epsilon)_s$ and $(\mathbf{q}_\epsilon)_v$ denote the scalar and vector part of the quaternion $\mathbf{q}_\epsilon$, respectively, see the notation section if necessary. $\boldsymbol{\phi}_{1j}(\boldsymbol{s}_j) = \lfloor \boldsymbol{s}_j \rceil^{1/2} + \boldsymbol{\beta}_j\boldsymbol{s}_j$ and $\boldsymbol{\phi}_{2j}(\boldsymbol{s}_j) = \frac{1}{2}\lfloor \boldsymbol{s}_j \rceil^0 + \frac{3}{2}\boldsymbol{\beta}_j\lfloor \boldsymbol{s}_j \rceil^{1/2} + \boldsymbol{\beta}_j^2\boldsymbol{s}$ are diagonal matrix functions, where $\lfloor \boldsymbol{s}_j \rceil^q = |\boldsymbol{s}_j|^q sign(\boldsymbol{s}_j)$, for $j \in \{\tau, f\}$. $\boldsymbol{K}_j, \boldsymbol{\alpha}_{ij}, \boldsymbol{\beta}_j \in \mathbb{R}^3, i = 1,2,\ j \in \{\tau, f\}$ are diagonal gain matrices to be designed. $\boldsymbol{s}_\tau$ and $\boldsymbol{s}_f$ denote sliding surfaces that are defined according to:

$$\boldsymbol{s}_\tau = \boldsymbol{\omega}_c^{(c)} + \boldsymbol{K}_\tau(\mathbf{q}_\epsilon)_v \tag{42}$$

$$\boldsymbol{s}_f = \dot{\boldsymbol{r}}_\epsilon^{(c)} + \boldsymbol{K}_f\boldsymbol{r}_\epsilon^{(c)} \tag{43}$$

It should be pointed out that the choice of the GSTA is motivated by the fact that its stability face to (matched) state-dependent disturbances is formally proved, as opposed to the STA. This is the case there, see (50)-(53).

Now, let us include the following assumption:

Assumption 3. *Let* $\boldsymbol{\varphi} = \left[\left(\boldsymbol{J}^{-1}\boldsymbol{\tau}_\Delta\right)^T \quad \frac{1}{m}\boldsymbol{f}_\Delta^T\right]^T$ *be a vector of perturbations, that depends on a vector* $\boldsymbol{s}$*, a function of* $\boldsymbol{q}_c, \boldsymbol{\omega}_c^{(c)}, \boldsymbol{r}_e^{(c)}, \dot{\boldsymbol{r}}_e^{(c)}$ *(*$\boldsymbol{s}$ *will be the sliding surface later). It is assumed that* $\|\partial\boldsymbol{\varphi}/\partial t\|_\infty \leq \delta_1$ *and* $\|\partial\boldsymbol{\varphi}/\partial\boldsymbol{s}\|_\infty \leq \delta_2$.

This assumption states that the first derivatives of the fault estimation error versus time and the sliding surface, are bounded, in the l_∞-norm sense (maximum magnitude).

The following theorem provides the solution to the design of $\boldsymbol{K}_j, \boldsymbol{\alpha}_{ij}, \boldsymbol{\beta}_j \in \mathbb{R}^3, i = 1,2,\ j \in \{\tau, f\}$.

Theorem 4. *Under assumption 3, the control law (40)-(43) ensures asymptotic stability and trajectory tracking, despite the presence of the state-dependent perturbations* $\boldsymbol{\tau}_\Delta$ *and* $\boldsymbol{f}_\Delta$*, if* $\boldsymbol{K}_\tau > 0, \boldsymbol{K}_f > 0$ *and if there exists any* $\kappa > 0$*,* $\boldsymbol{\alpha}_{1\tau}, \boldsymbol{\alpha}_{1f}, \boldsymbol{\alpha}_{2\tau}, \boldsymbol{\alpha}_{2f}, \boldsymbol{\beta}_\tau$ *and* $\boldsymbol{\beta}_f$ *such that:*

$$\alpha_{1i} > \frac{2(1+\kappa)\delta_2}{\beta_i},\ \alpha_{2i} > \frac{1}{4h_i\kappa}\left(2\delta_1\frac{1+\kappa}{\alpha_{1i}} + \frac{\kappa\delta_2}{\beta_i}\right)^2 + 2\delta_1 \tag{44}$$

$$h_i = 1 - \frac{\delta_2(1+\kappa)}{\beta_i\alpha_{1i}} \quad i = \overline{1,6} \tag{45}$$

$$\boldsymbol{\alpha}_j = diag\left(\boldsymbol{\alpha}_{j\tau}, \boldsymbol{\alpha}_{jf}\right) = diag(\alpha_{ji}) \quad j = 1,2 \quad i = \overline{1,6} \tag{46}$$

$$\boldsymbol{\beta} = diag\left(\boldsymbol{\beta}_\tau, \boldsymbol{\beta}_f\right) = diag(\beta_i) \quad i = \overline{1,6} \tag{47}$$

Proof

- Conditions on $\boldsymbol{\alpha}_{1\tau}, \boldsymbol{\alpha}_{1f}, \boldsymbol{\alpha}_{2\tau}, \boldsymbol{\alpha}_{2f}, \boldsymbol{\beta}_\tau$ *and* $\boldsymbol{\beta}_f$*:* Consider the definition of the sliding surface (42). Then, it follows from (38) that

$$\begin{aligned}\dot{\boldsymbol{s}}_\tau =& \dot{\boldsymbol{\omega}}_c^{(c)} + \boldsymbol{K}_\tau(\dot{\mathbf{q}}_\epsilon)_v = \boldsymbol{F}_\tau + \boldsymbol{J}^{-1}\left(\boldsymbol{\tau}_{sm}^{(c)} + \boldsymbol{\tau}_\Delta^{(c)}\right)\\ &+ \boldsymbol{K}_\tau\left[\frac{1}{2}\left[(\mathbf{q}_\epsilon)_s\boldsymbol{\omega}_c^{(c)} + (\mathbf{q}_\epsilon)_v \times \boldsymbol{\omega}_c^{(c)}\right]\right]\end{aligned} \tag{48}$$

Substituting (40) into (48) leads to

$$\dot{\boldsymbol{s}}_\tau = -\boldsymbol{\alpha}_{1\tau}\boldsymbol{\phi}_{1\tau}(\boldsymbol{s}_\tau) - \boldsymbol{\alpha}_{2\tau}\int_0^t \boldsymbol{\phi}_{2\tau}(\boldsymbol{s}_\tau(\chi))d\chi + \boldsymbol{J}^{-1}\boldsymbol{\tau}_\Delta \tag{49}$$

Now, consider the auxiliary variable $\boldsymbol{z}_\tau = -\boldsymbol{\alpha}_{2\tau}\int_0^t \boldsymbol{\phi}_{2\tau}(\boldsymbol{s}_\tau(\chi))d\chi + \boldsymbol{J}^{-1}\boldsymbol{\tau}_\Delta$. Then, (49) can be rewritten according to the following

pair of differential equations:

$$\dot{\boldsymbol{s}}_\tau = -\boldsymbol{\alpha}_{1\tau}\boldsymbol{\phi}_{1\tau}(\boldsymbol{s}_\tau) + \boldsymbol{z}_\tau \tag{50}$$

$$\dot{\boldsymbol{z}}_\tau = -\boldsymbol{\alpha}_{2\tau}\boldsymbol{\phi}_{2\tau}(\boldsymbol{s}_\tau) + \boldsymbol{J}^{-1}\dot{\boldsymbol{\tau}}_\Delta \tag{51}$$

Similarly, it can be verified that the following equations can be derived from (41) and (43):

$$\dot{\boldsymbol{s}}_f = -\boldsymbol{\alpha}_{1f}\boldsymbol{\phi}_{1f}(\boldsymbol{s}_f) + \boldsymbol{z}_f \tag{52}$$

$$\dot{\boldsymbol{z}}_f = -\boldsymbol{\alpha}_{2f}\boldsymbol{\phi}_{2f}(\boldsymbol{s}_f) + \frac{1}{m}\dot{\boldsymbol{f}}_\Delta \tag{53}$$

with $\boldsymbol{z}_f = -\boldsymbol{\alpha}_{2f}\int_0^t \boldsymbol{\phi}_{2f}(\boldsymbol{s}_f(\chi))d\chi + \frac{1}{m}\boldsymbol{f}_\Delta$.

It is now fundamental to remind that $\boldsymbol{\tau}_\Delta$ and $\boldsymbol{f}_\Delta$ depend on both the rotational and translational states. Then (50)-(53) are coupled, but this coupling is lumped in the perturbation terms $\dot{\boldsymbol{\tau}}_\Delta$ and $\dot{\boldsymbol{f}}_\Delta$. For the design of the GSTA's parameters, it doesn't matter the role of these terms if we can guarantee stability, considering the state-dependent property of $\dot{\boldsymbol{\tau}}_\Delta$ and $\dot{\boldsymbol{f}}_\Delta$.

To proceed, let us merge (50)-(53) together according to:

$$\dot{\boldsymbol{s}} = -\boldsymbol{\alpha}_1\boldsymbol{\phi}_1(\boldsymbol{s}) + \boldsymbol{z} \tag{54}$$

$$\dot{\boldsymbol{z}} = -\boldsymbol{\alpha}_2\boldsymbol{\phi}_2(\boldsymbol{s}) + \dot{\boldsymbol{\varphi}}(\boldsymbol{s}) \tag{55}$$

with $\boldsymbol{s} = \begin{bmatrix}\boldsymbol{s}_\tau^T & \boldsymbol{s}_f^T\end{bmatrix}^T$, $\boldsymbol{z} = \begin{bmatrix}\boldsymbol{z}_\tau^T & \boldsymbol{z}_f^T\end{bmatrix}^T$, $\boldsymbol{\varphi} = \begin{bmatrix}\left(\boldsymbol{J}^{-1}\boldsymbol{\tau}_\Delta\right)^T & \frac{1}{m}\boldsymbol{f}_\Delta^T\end{bmatrix}^T$, $\boldsymbol{\alpha}_1 = \text{diag}\left(\boldsymbol{\alpha}_{1\tau}, \boldsymbol{\alpha}_{1f}\right)$ and $\boldsymbol{\alpha}_2 = \text{diag}\left(\boldsymbol{\alpha}_{2\tau}, \boldsymbol{\alpha}_{2f}\right)$. Noticing that each matrix and matrix functions that enter in this equation have a diagonal structure and $\dot{\boldsymbol{\varphi}}(\boldsymbol{s}) = \frac{\partial \boldsymbol{\varphi}}{\partial t} + \left(\frac{\partial \boldsymbol{\varphi}}{\partial \boldsymbol{s}}\right)\dot{\boldsymbol{s}}$, it follows under assumption 3, that direct application of Corollary 1 in [4] leads to the conditions (44)-(47).

- *Conditions on $\boldsymbol{K}_\tau$ and $\boldsymbol{K}_f$:* Once $\boldsymbol{s}_\tau = 0$ is reached, $\boldsymbol{\omega}_c^{(c)} = -\boldsymbol{K}_\tau(\mathbf{q}_\epsilon)_v$. Consider the following Lyapunov function:

$$V_\tau = [1 - (\mathbf{q}_\epsilon)_s]^2 + (\mathbf{q}_\epsilon)_v^T(\mathbf{q}_\epsilon)_v \tag{56}$$

Differentiating V_τ versus time, it follows:

$$\begin{aligned}
\dot{V}_\tau =& -2[1 - (\mathbf{q}_\epsilon)_s](\dot{\mathbf{q}}_\epsilon)_s + 2(\mathbf{q}_\epsilon)_v^T(\dot{\mathbf{q}}_\epsilon)_v \\
=& -2[1 - (\mathbf{q}_\epsilon)_s][-\frac{1}{2}(\mathbf{q}_\epsilon)_v^T\boldsymbol{\omega}_c^{(c)}] + 2(\mathbf{q}_\epsilon)_v^T\frac{1}{2}[(q_\epsilon)_s\boldsymbol{\omega}_c^{(c)} + \\
& (\mathbf{q}_\epsilon)_v \times \boldsymbol{\omega}_c^{(c)}] \\
=& -2[-\frac{1}{2}(\mathbf{q}_\epsilon)_v^T\boldsymbol{\omega}_c^{(c)} + \frac{1}{2}(\mathbf{q}_\epsilon)_s(\mathbf{q}_\epsilon)_v^T\boldsymbol{\omega}_c^{(c)}] + 2(\mathbf{q}_\epsilon)_v^T\frac{1}{2}[(\mathbf{q}_\epsilon)_s\boldsymbol{\omega}_c^{(c)} + \\
& (\mathbf{q}_\epsilon)_v \times \boldsymbol{\omega}_c^{(c)}] \\
=& -[(\mathbf{q}_\epsilon)_v^T\boldsymbol{K}_\tau(\mathbf{q}_\epsilon)_v - (\mathbf{q}_\epsilon)_s(\mathbf{q}_\epsilon)_v^T\boldsymbol{K}_\tau(\mathbf{q}_\epsilon)_v] - (\mathbf{q}_\epsilon)_v^T(\mathbf{q}_\epsilon)_s\boldsymbol{K}_\tau(\mathbf{q}_\epsilon)_v \\
=& -(\mathbf{q}_\epsilon)_v^T\boldsymbol{K}_\tau(\mathbf{q}_\epsilon)_v
\end{aligned} \tag{57}$$

which is strictly definite negative iff $\boldsymbol{K}_\tau > 0$.

Similarly, once $\boldsymbol{s}_f = 0$ is reached, $\dot{\boldsymbol{r}}_\epsilon^{(c)} = -\boldsymbol{K}_f\boldsymbol{r}_\epsilon^{(c)}$ which is an autonomous linear differential equation and then, stable, iff $\boldsymbol{K}_f > 0$, which terminates the proof. □

5.3. The anti-windup system

If equations (40) and (41) are directly used as the control law, saturation caused by the integral term may lead to a severe overshoot in the system, or provoke instability of the closed loops. This point becomes especially crucial when dealing with FTC problem, since faults may cause actuator saturation. Here, anti-windup coefficients of the general form $e^{\lambda\Delta_i}, \lambda < 0$ are introduced in (40) and (41) as follows:

$$\begin{aligned}
\boldsymbol{\tau}_{sm}^{(c)} =& \boldsymbol{J}\Big(-\boldsymbol{F}_\tau - \boldsymbol{K}_\tau\Big[\frac{1}{2}\left[(\mathbf{q}_\epsilon)_s\boldsymbol{\omega}_c^{(c)} + (\mathbf{q}_\epsilon)_v \times \boldsymbol{\omega}_c^{(c)}\right]\Big] \\
& -\boldsymbol{\alpha}_{1\tau}\boldsymbol{\phi}_{1\tau}(\boldsymbol{s}_\tau) - \boldsymbol{\alpha}_{2\tau}\text{diag}(e^{\lambda\Delta_{\tau i}})\int_0^t \boldsymbol{\phi}_{2\tau}(\boldsymbol{s}_\tau(\chi))d\chi\Big)
\end{aligned} \tag{58}$$

$$\begin{aligned}
\boldsymbol{f}_{sm}^{(c)} =& m\Big(-\boldsymbol{F}_f - \boldsymbol{K}_f\dot{\boldsymbol{r}}_\epsilon^{(c)} - \boldsymbol{\alpha}_{1f}\boldsymbol{\phi}_{1f}(\boldsymbol{s}_f) \\
& -\boldsymbol{\alpha}_{2f}\text{diag}(e^{\lambda\Delta_{fi}})\int_0^t \boldsymbol{\phi}_{2f}(\boldsymbol{s}_f(\chi))d\chi\Big), \quad i = \overline{1,3}
\end{aligned} \tag{59}$$

To explain the role of $\lambda, \Delta_{\tau i}, \Delta_{fi}$, $i = \overline{1,3}$, let us recall that the thruster configuration consists of 24 thrusters of $2N$. Then, the control vector $\boldsymbol{u}_c^{(c)}$ ranges in a hypercube of dimension 24. The images of this hypercube through the thruster configuration matrices $\boldsymbol{R}_\tau$ and $\boldsymbol{R}_f$ (see eq. (25)) are polytopes $\boldsymbol{\Pi}_\tau$ and $\boldsymbol{\Pi}_f$ that can be computed through linear algebra. These polytopes are nothing else than the torque and force domains, that can be attained by the actuation unit. Thus, saturation occurs if a torque and/or a force outside of $\boldsymbol{\Pi}_\tau$ and $\boldsymbol{\Pi}_f$, is asked to be allocated on the thrusters, see Fig. 5 that gives an illustration for the torque case.

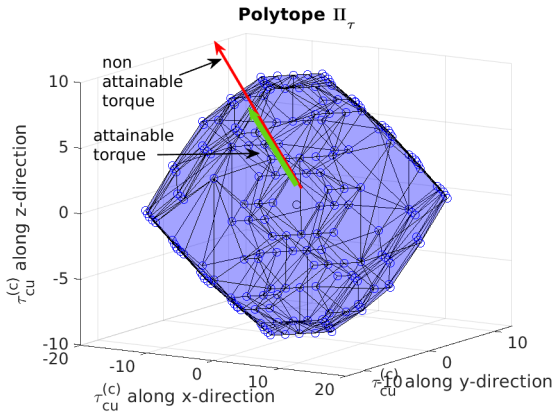

Figure 5: The polytope $\boldsymbol{\Pi}_\tau$ (attainable torque domain)

If saturation occurs, which means that $\boldsymbol{\tau}_{FTC}^{(c)}$ and/or $\boldsymbol{f}_{FTC}^{(c)}$ are outside $\boldsymbol{\Pi}_\tau$ and/or $\boldsymbol{\Pi}_f$, then the nearest attainable torque and/or force that belongs to $\boldsymbol{\Pi}_\tau/\boldsymbol{\Pi}_f$, is computed, in the least square optimal sense. To formulate this problem, let us denote $\boldsymbol{\tau}_0^{(c)}$ and $\boldsymbol{f}_0^{(c)}$ these optimal attainable torque and force. Then, the problem turns out to solve on-line, the following optimisation

problems

$$\min_{\boldsymbol{\tau}_0^{(c)}} \left\| \boldsymbol{\tau}_{FTC}^{(c)} - \boldsymbol{\tau}_0^{(c)} \right\|_2 \quad \text{s.t.} \quad \boldsymbol{\tau}_0^{(c)} \in \boldsymbol{\Pi}_\tau$$
$$\min_{\boldsymbol{f}_0^{(c)}} \left\| \boldsymbol{f}_{FTC}^{(c)} - \boldsymbol{f}_0^{(c)} \right\|_2 \quad \text{s.t.} \quad \boldsymbol{f}_0^{(c)} \in \boldsymbol{\Pi}_f \tag{60}$$

The terms $\Delta_{\tau i}, \Delta_{fi}$, $i = \overline{1,3}$ are then defined according to:

$$\boldsymbol{\Delta}_\tau = \boldsymbol{\tau}_{FTC}^{(c)} - \boldsymbol{\tau}_0^{(c)} \quad \boldsymbol{\Delta}_f = \boldsymbol{f}_{FTC}^{(c)} - \boldsymbol{f}_0^{(c)} \tag{61}$$
$$\boldsymbol{\Delta}_\tau = \text{vec}(\Delta_{\tau i}),\ \boldsymbol{\Delta}_f = \text{vec}(\Delta_{fi}),\ \Delta_{\tau i} \geq 0, ,\ \Delta_{fi} \geq 0 \quad i = \overline{1,3}$$

Thus, with $\lambda < 0$, when $\Delta_{\tau i}/\Delta_{fi}$ is large enough for some "i", $e^{\lambda \Delta_{\tau i}}/e^{\lambda \Delta_{fi}}$ is near zero according to the property of the exponential function, vanishing the integral terms in the GSTA. *A contrario*, provided that the system is not saturated, $\boldsymbol{\tau}_0^{(c)} = \boldsymbol{\tau}_{FTC}^{(c)}$ and $\boldsymbol{f}_0^{(c)} = \boldsymbol{f}_{FTC}^{(c)}$. Then, the value of $e^{\lambda \Delta_{\tau i}}/e^{\lambda \Delta_{fi}}$, $i = \overline{1,3}$ is invariant and equal to 1, no matter how the GSTA will react to faults, the integral terms operate normally.

6. Simulation results

The performances of the proposed FTC architecture are next assessed using the FES. A path planning algorithm has been implemented to generate smooth attitude quaternion $\mathbf{q}_{ref}(t)$ and relative position $\boldsymbol{r}_{ref}^{(c)}(t)$ references. We recall that the rendezvous trajectory consists of:

i) a chaser's rotation around its center-of-mass to align the capture mechanism with the target (we denote it "alignment phase" in the following figures). The time duration of this phase is $300s$.

ii) a chaser's translation of approximatively $100m$ along the y-axis, into the direction of the target to capture it (we refer to it as the "forced translation phase"). In this phase, the attitude is controlled to keep the capture mechanism aligned with the target . The time duration of this phase is $1200s$.

For each simulation, the initial position of the chaser corresponds to the initial orbital parameters given in Table 1, i.e. the chaser is approximatively $100m$ behind the target along the y-axis. The initial attitude is $30deg$ along the y-axis, and $0deg$ along the x- and z-axis. The initial angular velocity of the chaser is null along all axis. For each phase, the path planning algorithm uses a second order spline function of the time t. Thus, the components of $\mathbf{q}_{ref}(t)$ and $\boldsymbol{r}_{ref}^{(c)}(t)$ are given by the following function,

$$h(t) = \begin{cases} h_0 & \text{if } t \leq t_i \\ \frac{h_0}{2\left(\frac{t_f - t_i}{2}\right)^2} t^2 - h_0 & \text{if } t_i \leq t \leq \frac{t_f - t_i}{2} \\ -\frac{x_0 \left(t + t_i - t_f\right)^2}{2\left(\frac{t_f - t_i}{2}\right)^2} & \text{if } \frac{t_f - t_i}{2} \leq t \leq t_f \\ 0 & \text{if } t \geq t_f \end{cases} \tag{62}$$

where h_0 refers to the initial value of h. Note that this algorithm considers the fact that the final relative position and the final attitude are equal to 0 (in the adequate frame).

Following Theorem 4, the GSTA (40)-(41) is characterized by the parameters $\boldsymbol{K}_\tau, \boldsymbol{K}_f, \boldsymbol{\alpha}_{1\tau}, \boldsymbol{\alpha}_{1f}, \boldsymbol{\alpha}_{2\tau}, \boldsymbol{\alpha}_{2f}, \boldsymbol{\beta}_\tau, \boldsymbol{\beta}_f$. These parameters are tuned in this work, according to the following reasoning:

• $\boldsymbol{\alpha}_{1\tau}, \boldsymbol{\alpha}_{1f}, \boldsymbol{\alpha}_{2\tau}, \boldsymbol{\alpha}_{2f}, \boldsymbol{\beta}_\tau, \boldsymbol{\beta}_f$: The bounds δ_1 and δ_2 being determined according to Assumption 3, $\boldsymbol{\alpha}_{1\tau}, \boldsymbol{\alpha}_{1f}, \boldsymbol{\alpha}_{2\tau}, \boldsymbol{\alpha}_{2f}$ are computed following equations (44)- (47), once $\boldsymbol{\beta}_\tau$ and $\boldsymbol{\beta}_f$ are fixed. $\boldsymbol{\beta}_\tau, \boldsymbol{\beta}_f$ are related to growing terms $\frac{3}{2}\boldsymbol{\beta}_j \lfloor \boldsymbol{s}_j \rceil^{1/2}$ and $\boldsymbol{\beta}_j^2 s$ in functions $\boldsymbol{\phi}_{2j}(\boldsymbol{s}_j)$, $j \in \{\tau, f\}$, that help to counteract the effects of the state dependent perturbations $\boldsymbol{\varphi} = \left[\left(\boldsymbol{J}^{-1}\boldsymbol{\tau}_\Delta\right)^T \ \frac{1}{m}\boldsymbol{f}_\Delta^T \right]^T$. Thus $\boldsymbol{\beta}_\tau, \boldsymbol{\beta}_f$ are determined in this work, by seeking the behaviour of each component of $\boldsymbol{\varphi}$ in simulations, which leads to $\boldsymbol{\beta}_\tau = \boldsymbol{\beta}_f = \text{diag}(1, 1.1, 1).10^{-4}$. Of course, these values are determined approximatively and we cannot expect to obtain an optimal tuning using this practical approach. The application of formulas (44)- (47) leads to:

$$\boldsymbol{\alpha}_{1\tau} \approx \text{diag}(0.002145, 0.001898, 0.002487)$$
$$\boldsymbol{\alpha}_{2\tau} \approx \text{diag}(0.3373, 0.264, 0.4539).10^{-3}$$
$$\boldsymbol{\alpha}_{1f} \approx \text{diag}(0.05056, 0.03464, 0.04609)$$
$$\boldsymbol{\alpha}_{2f} \approx \text{diag}(0.01875, 0.0088, 0.01558)$$

• $\boldsymbol{K}_\tau, \boldsymbol{K}_f$: It can be seen from the second part of the proof of Theorem 4, that $\boldsymbol{K}_\tau, \boldsymbol{K}_f$ play the role of dynamic evolution matrices. So, their eigenvalues have the sense of the dynamics of the closed-loop. $\boldsymbol{K}_\tau$ and $\boldsymbol{K}_f$ are thus fixed to $\boldsymbol{K}_\tau = \boldsymbol{K}_f = \mathbb{I}_3$, meaning that it is required a bandwidth of the closed-loop equal to $1rd/s$. By such a choice, the solar array and the propellant sloshing modes are in the bandwidth of the control. Of course, the price to pay will be an increase in the control energy consumption.

6.1. The perfect navigation unit case

We first consider two simulations under a perfect navigation unit, i.e. the measurements provided by the navigation unit are nothing else than the variables that enter in the disturbance/fault estimator and the GSTA. The goal is to make the readers clearly understand the results.

6.1.1. Additive fault type

Let us consider the (simple) case of an additive fault type. The faulty scenario consists of a sinus signal added to the thruster's firing N. 16, from $t = 1000s$ until the simulation's end. The magnitude and the frequency of the sinus are fixed to $a_0 = 0.15N$ and $\varphi_0 = 0.01rd/s$, see (29). With such a choice, the anti-windup strategy will not operate, since the control commands will not attain their saturation levels. Fig. 6.a illustrates the chaser's attitude, and Fig. 6.b gives the relative position (in the LVLH frame). The attitude and relative position tracking errors are also plotted, to appreciate the results. The control commands $\boldsymbol{u}_c^{(c)}(t)$ applied to the thrusters, are illustrated in Fig. 7.a. The plots of the real thruster's firings applied to the spacecraft, are given in Fig. 7.b. The total control signal provided by the overall FTC scheme (dual force $\bar{\boldsymbol{f}}_{FTC}^{(c)}(t)$), the fault/disturbance

dual force estimate $\bar{\hat{f}}^{(c)}(t)$ and the dual force $\bar{f}^{(c)}_{sm}(t)$ delivered by the GSTA controllers, are shown in Fig. 8.

The most notable result is probably the fact that the harmonic component of the fault is visible in the fault/disturbance dual force estimate $\bar{\hat{f}}^{(c)}(t)$, see Fig. 8.b. Since $\bar{f}^{(c)}_{FTC} = \bar{f}^{(c)}_{sm} - \bar{\hat{f}}^{(c)}$, this harmonic is also visible in $\bar{f}^{(c)}_{FTC}(t)$. Furthermore, due to the sign, the sine behaviour is in opposite phase between $\bar{\hat{f}}^{(c)}$ and $\bar{f}^{(c)}_{FTC}$, see Fig. 8.a and Fig. 8.b. Note that the sine component is transmitted to all thrusters through the CA unit, see Fig. 7.a. Such results are clearly reassuring about the functioning of all sub-elements of the proposed FTC architecture.

In terms of mission performance, during the alignment phase, the attitude error does not exceed 0.4 deg and the relative position is less than 2 cm. During the forced translation phase and at the capture point, these errors are very close to zero. Furthermore, it can be seen on Fig.7.a that these performances are obtained without actuator saturation. It can be observed a periodic behaviour of $u^{(c)}_c(t)$ at frequencies that correspond to the flexible modes of the solar array and propellant sloshing. This is coherent with the choice of the GSTA parameters listed previously. In terms of propellant consumption, a total of 1.83kg is used. The impulse per unit weight-on-Earth of the 24 thrusters has been fixed to $I_{sp} = 210s$. Thus, we argue from the presented figures that the obtained results are promising, since the rendezvous and capture performances are met whenever the fault occurrence, but the price to pay is about the propellant consumption.

6.1.2. *Stuck open fault*

Let us now consider the case of a stuck-open fault occurring in thruster N. 1. In the simulated scenario, the fault occurs at $t = 40s$. The time of fault occurrence is chosen to cover both the acquisition and translation phases. It enables to analyse the behaviour of the spacecraft when it rotates simultaneously around its 3 axis, while performing at the same time a translation in 3 dimensions. Such a manoeuvre enables to evaluate the 6-DOF capacity of the proposed FTC solution. Note that the stuck open fault type corresponds to a totally unavailable actuator, which is a more severe fault than the previous one. The obtained results are given in Fig. 9 to 11.

As it can be seen, during the rotation phase, the attitude error does not exceed 0.4 deg and the relative position is less than 5 cm. During the forced translation phase and at the capture point, these errors are very close to zero. Furthermore, it can be seen in Fig. 10.a that these performances are obtained without actuator saturation, except during a short time which corresponds to the transient behaviour of the FTC algorithm to accommodate the fault. Thanks to the anti-windup strategy, this does not cause instability of the FTC scheme. Note that, without the anti-windup scheme, it has been observed an instability of the FTC law. These results are not presented in this article, since they do not really provide useful information. In terms of propellant consumption, a total of 6.62kg is used. Thus, again, we argue from the presented figures that the obtained results are promising, since the rendezvous and capture performances are satisfied, despite a totally uncontrollable thruster, but there is a price to pay in terms of propellant consumption.

6.2. *Navigation unit in the loop*

We now investigate the performance of the FTC scheme, by analysing the same faulty situation, considering the navigation unit in the loop. Fig. 12 to 14 show the results. Of course, navigation errors and measurement noises affect especially the control signals, say dramatically, which is a well-known shortcoming of sliding mode techniques, see Fig. 13 and 14. However, despite this phenomenon, the capture performances are satisfactory, since during the last 10 meters, the attitude error does not exceed 0.05 deg and the relative position is less than 1 cm along the three axes. The total propellant consumption is estimated to 9.5kg, which is coherent with the behaviour of the control signals. However, the capture mission is a success.

6.3. *Simulation campaign with the FES*

The proposed FTC solution is finally evaluated through a simulation campaign using the FES, see Fig. 15 to 17. A total of 48 faulty scenes were tested. The fault type is chosen randomly between additive sinus faults, loss-of-effectiveness, stuck-open and stuck-closed faults. We recall that the cases of stuck-open and stuck-closed faults correspond respectively, to a positive and negative drift that substitutes the control signals at the actuator level, see Fig. 3. For the additive sinus fault type, a sinus is added to the thruster's command. Loss-of-effectiveness corresponds simply to a gain variation. The key ingredient of the considered scenes is that faults occur at the thruster firing level. The simulations are performed so that all the 24 thrusters are covered twice. However, all fault occurrences have been fixed to $t = 40s$. We recall that the challenges of the considered scenarios, are:

- stuck-open and stuck-closed faults have abrupt profiles and correspond to totally uncontrollable actuators, after some very short transient time. Thus, the fault profile is not continuous, which contradicts the assumptions made in most sliding-mode control techniques. However, the first derivatives versus time and the sliding surface of the fault estimation error, are required to be bounded, in the l_∞-norm sense, see Assumption 3.
- the faults may cause actuator saturation, which may provoke instability of the closed-loops due to the presence of the integral term in (40)-(41). Thanks to the antiwindup solution (58)-(59), this problem is solved.
- the considered fault patterns correspond to the known on-orbit failures occurred in some real missions, see Table 3.

The performance are evaluated using the following mission-oriented criteria:

- Dealing with relative position and velocity, it is required to maintain the relative position inside the so-called rendezvous corridor, during the complete forced translation phase, see Fig. 16.a At the capture point, the position misalignment must be less than 20 cm along the X and Y axes, see Fig. 15.a, and

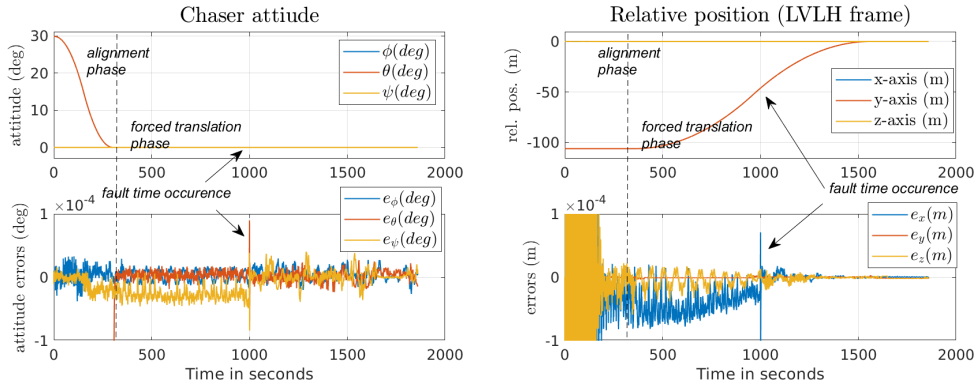

Figure 6: Perfect navigation and sine additive fault in THR 16: a) Attitude of the chaser - b) Relative position

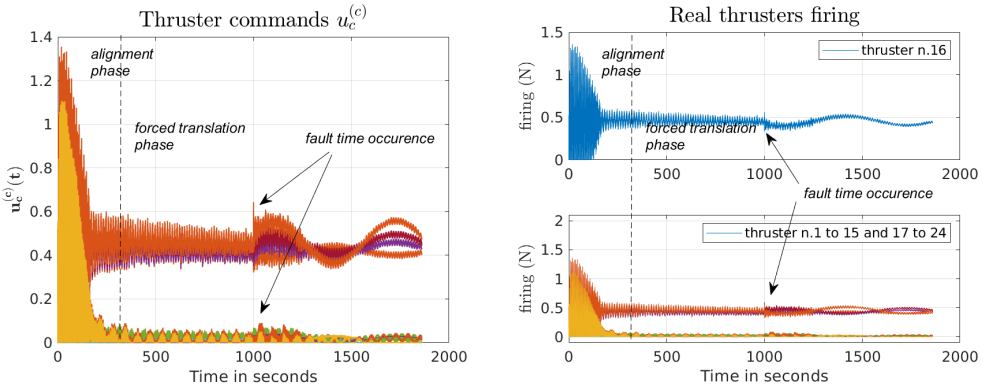

Figure 7: Perfect navigation and sine additive fault in THR 16: a) thruster commands $\boldsymbol{u}_c^{(c)}$ - b) real thruster's firing

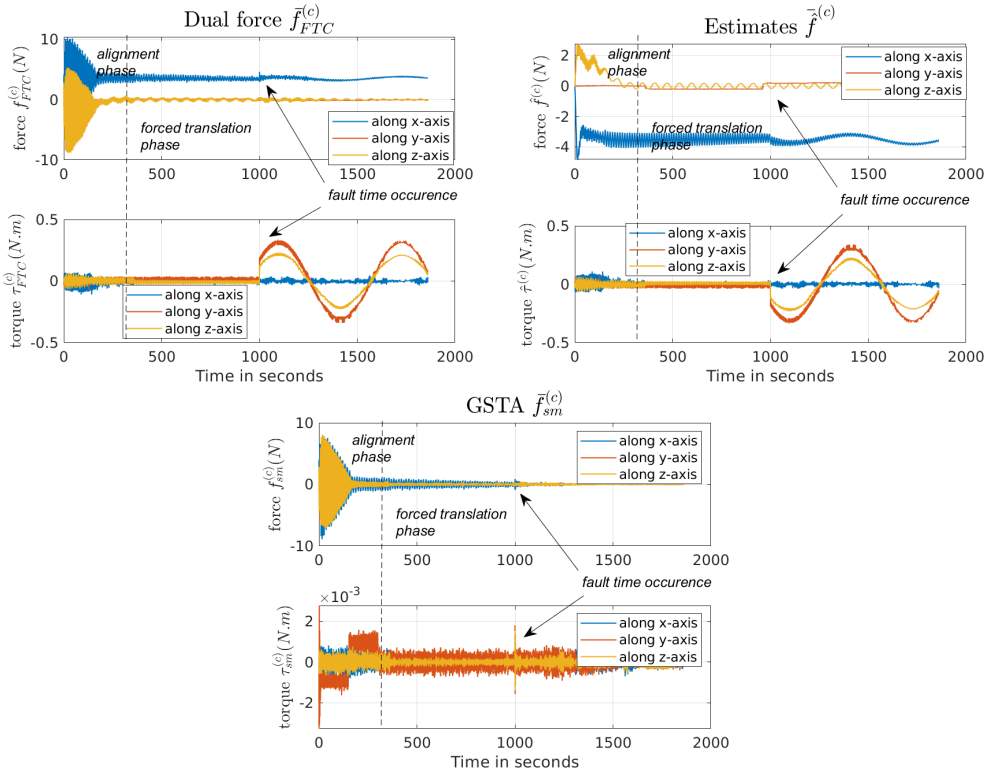

Figure 8: Perfect navigation and sine additive fault in THR 16: a) dual force $\bar{\boldsymbol{f}}_{FTC}^{(c)}$ - b) dual force estimate $\bar{\hat{\boldsymbol{f}}}^{(c)}$ - c) GSTA dual force $\bar{\boldsymbol{f}}_{sm}^{(c)}$

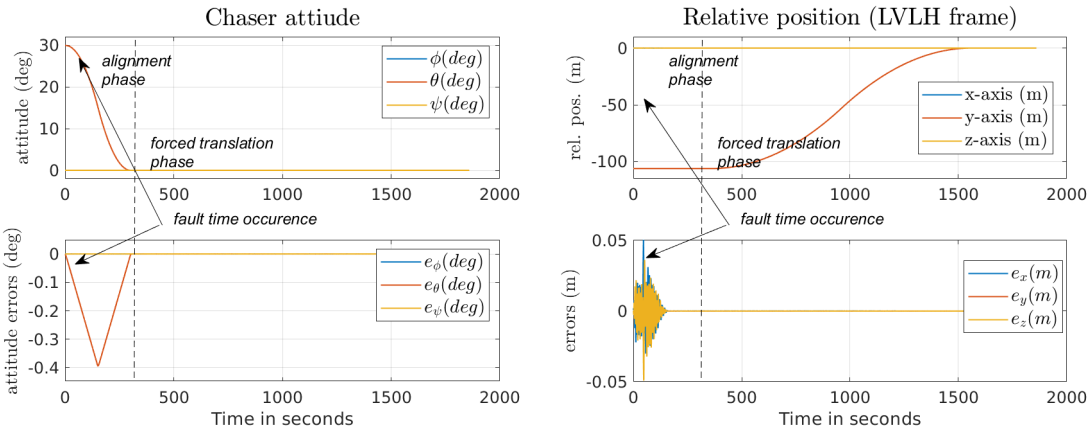

Figure 9: Perfect navigation and stuck-open fault in THR 1: a) Attitude of the chaser - b) Relative position

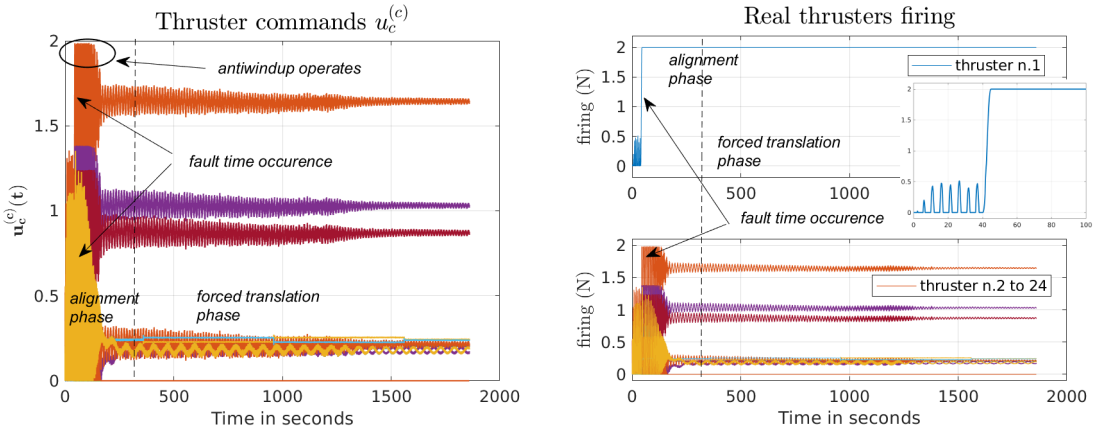

Figure 10: Perfect navigation and stuck-open fault in THR 1: a) thruster commands $\boldsymbol{u}_c^{(c)}$ - b) real thruster's firing

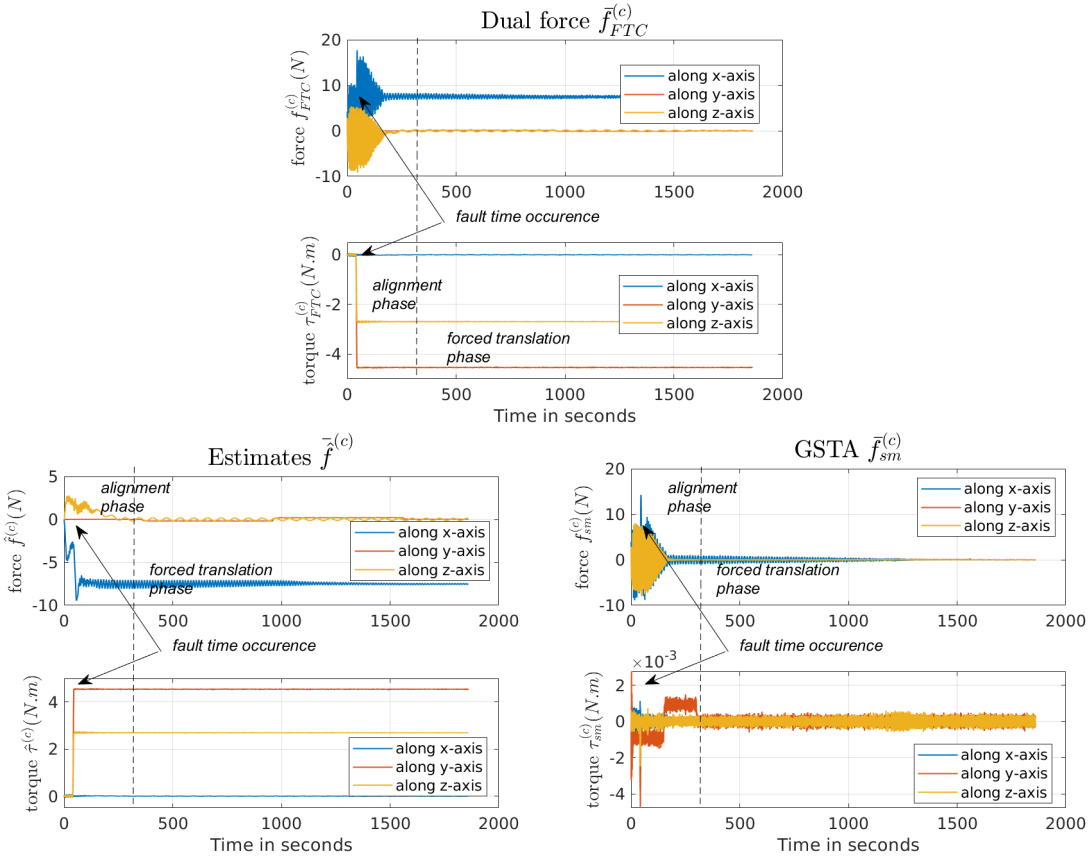

Figure 11: Perfect navigation and stuck-open fault in THR 1: a) dual force $\bar{\boldsymbol{f}}_{FTC}^{(c)}$ - b) dual force estimate $\bar{\hat{\boldsymbol{f}}}^{(c)}$ - c) GSTA dual force $\bar{\boldsymbol{f}}_{sm}^{(c)}$

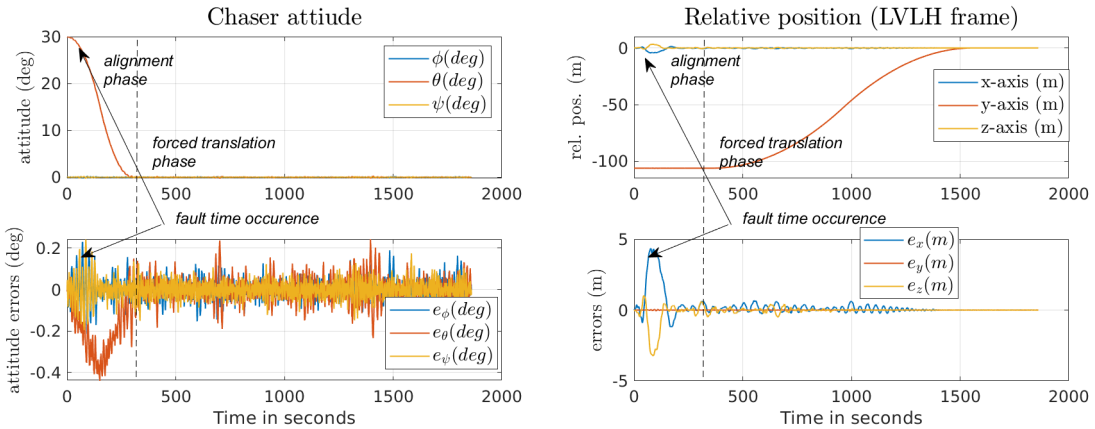

Figure 12: Navigation in the loop and stuck-open fault in THR 1: a) Attitude of the chaser - b) Relative position

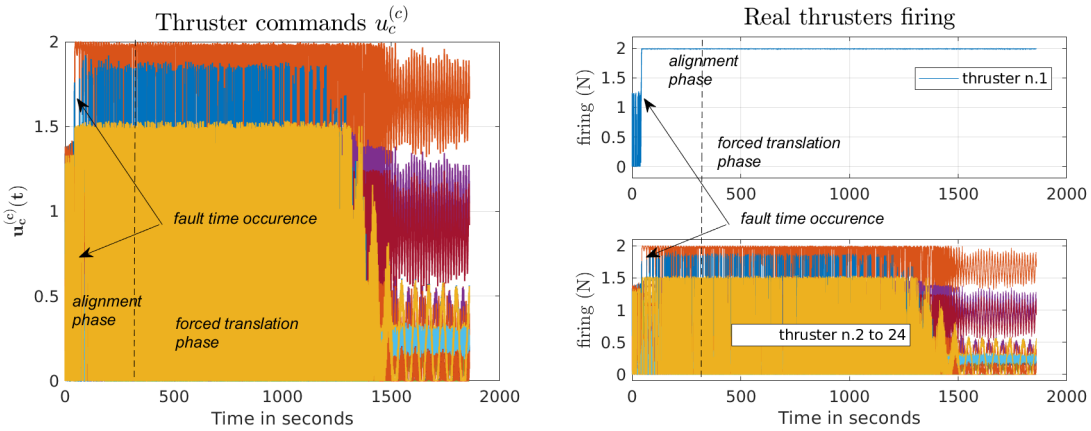

Figure 13: Navigation in the loop and stuck-open fault in THR 1: a) thruster commands $\boldsymbol{u}_c^{(c)}$ - b) real thruster's firing

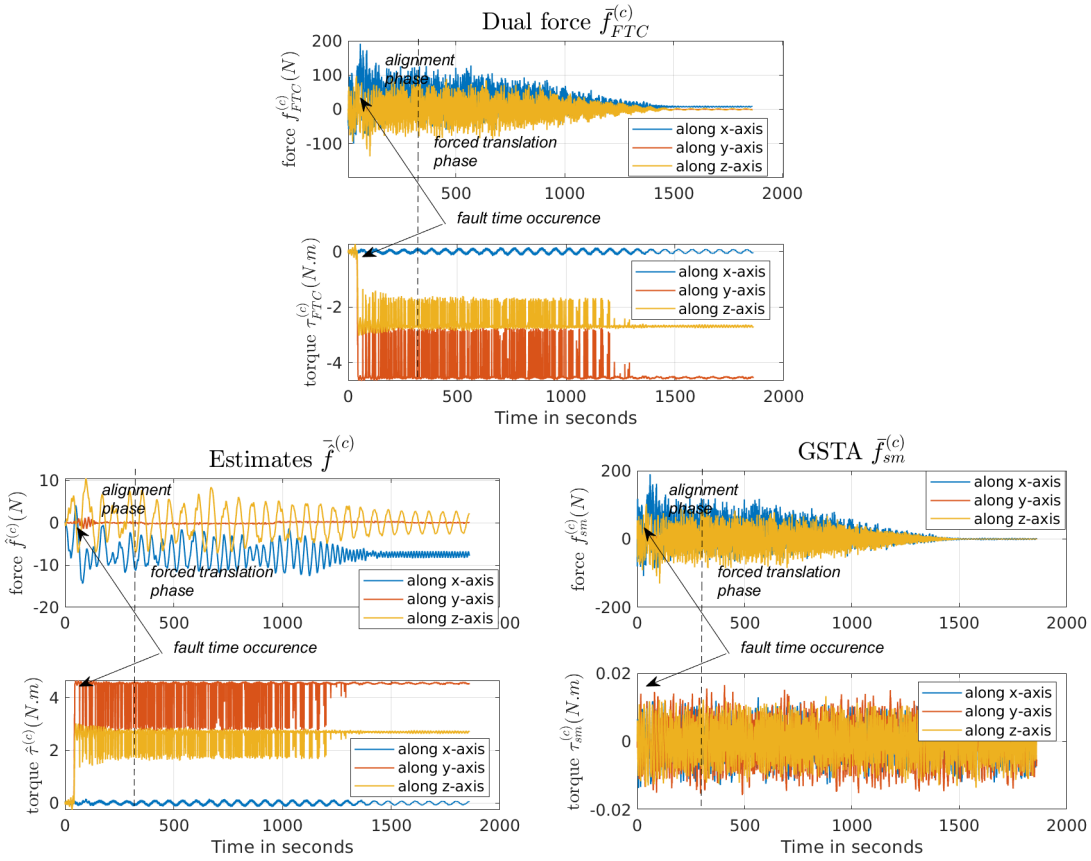

Figure 14: Navigation in the loop and stuck-open fault in THR 1: a) dual force $\bar{\boldsymbol{f}}_{FTC}^{(c)}$ - b) dual force estimate $\bar{\hat{\boldsymbol{f}}}^{(c)}$ - c) GSTA dual force $\bar{\boldsymbol{f}}_{sm}^{(c)}$

the lateral X and Y velocities must be less than 1 cm/s nominally, the worst case being fixed to 4 cm/s, see Fig. 15.b top. In terms of the longitudinal X-axis, the velocity must be less than 1 cm/s, see Fig. 15.b bottom.
• With regards to attitude performance, it is required after the alignment phase, to maintain the attitude to less than 1 deg along the three axes (pitch $\phi(t)$, yaw $\theta(t)$, roll $\psi(t)$) during the forced translation, see Fig. 16.b, so that the capture mechanism is correctly aligned with the target. At the capture point, the attitude misalignment must be less than 1 deg, see Fig. 17.a, and the angular rate must be less than 0.05 deg/s along the three axis, see Fig. 17.b.

These mission-oriented criteria enable to quantity the worst case of mission performance loss due to the faults. Particularly, it can be concluded from 15.b that the worst-cases correspond to stuck-closed faults that occur in thrusters 2, 4, 14 and 16. However, even for these cases, the capture performances are met.

6.4. Comparison with a FDI–based FTC solution

The obtained results are now compared with the FDI–based FTC solution proposed in [35]. This approach is retained since it has been validated under the GMV Space and Airbus Defence and Space demonstrator of the ESA's e.Deorbit mission. The method is based on:
• for fault diagnosis: a bank of nonlinear unknown input observers (NL-UIO) designed under a L_2-gain robustness constraint;
• for fault tolerance: control re-allocation technique.
The proposed strategy works as follows: as soon as the faulty thruster is isolated by the NL-UIO–based FDI unit, it is turned off using a dedicated pipe valve and the forces and torques computed by the controller are re-allocated among the healthy thrusters. For that purpose, the CA algorithm (26) is further constrained so that $0 \leq u_{c_j}^{(c)} \leq 0$, where j denotes the thrusters that have been identified to be faulty. In terms of control, the GSTA is used without the fault estimator (32) and (34). The anti-windup strategy (58)-(59) is kept in place.

The major difference with respect to the method proposed in this paper, is that the NL-UIO / CA FTC scheme operates at the thruster level, and not at the forces/torques level. The consequence is that the FDI unit is able to determine which subset of thrusters is faulty. This is a great advantage, see [22, 35] for more details. The solution unfortunately exhibits sensitiveness to false alarms, and then requires high robustness against especially the propellant sloshing and solar array flexible modes. A wrong decision from the FDI unit leads the CA unit *i*) to condemn a healthy thruster, and, *ii*) to think that the faulty thruster is still available for control. However, when the FDI unit succeeds, the FDI–based FTC approach prevents propellant consumption as opposed to the FE–based FTC solution proposed in this paper.
Fig.18 illustrates the results when the FDI–based FTC unit operates in spite of the FE–based FTC solution. The faulty scenario corresponds to the scenario considered in Section 6.1.2. Fig. 18.a-18.c illustrate the behaviour of the chaser's attitude, the relative position (in the LVLH frame) and the real thruster firing. Fig.18.d gives the propellant mass consumption for both the FTC solutions. As it can be seen, both FTC solutions lead to the same performance in terms of rendezvous and capture criteria. However, the FDI–based FTC solution exhibits less propellant consumption (a total of 1.82kg is used) than the FE–based FTC solution (6.62kg). The price to pay is about the complexity of the FDI unit that relies on 16 NL-UIOs of order 7, whereas the FE–based FTC scheme consists of the fault estimator (32) and (34).

7. Conclusions

This paper demonstrates that the generalized super-twisting algorithm combined with a nonlinear fault estimator, can successfully solve the problem of fault tolerance against thruster faults, for in-orbit autonomous rendezvous between a chaser spacecraft and a passive spacecraft. It is also demonstrated that an anti-windup strategy is required jointly with the fault-tolerant control unit to prevent instability due to actuator saturation when faults occur. The evaluation of mission-oriented criteria over 48 simulations under different faulty situations, demonstrates that the proposed solution accommodates a large class of actuator faults, including loss of controllability of the faulty actuator, despite the presence of uncertainties and disturbances. The advantage of the proposed solution concerning solutions that use fault detection and isolation procedures, consists of its insensitivity to false alarms and the reduced complexity required by the fault diagnosis algorithm. The price to pay is a high propellant consumption.

Acknowledgments

The authors gratefully acknowledge the financial support from CONACyT under grant 440473 (CVU 594664). J. Dávila gratefully acknowledges the financial support from SIP-IPN under grants 20200733 and 20210302.

References

[1] Alfriend, K., Vadali, S. R., Gurfil, P., How, J., Breger, L., 2009. Spacecraft formation flying: Dynamics, control and navigation. Vol. 2. Elsevier.
[2] Brodsky, V., Shoham, M., 1999. Dual numbers representation of rigid body dynamics. Mechanism and Machine Theory 34, 693–718.
[3] Cairano, S., Park, H., Kolmanovsky, I., 2012. Model predictive control approach for guidance of spacecraft rendezvous and proximity maneuvering. International Journal of Robust and Nonlinear Control 22 (12), 1398–1427.
[4] Castillo, I., Fridman, L., Moreno, J. A., 2018. Super-twisting algorithm in presence of time and state dependent perturbations. International Journal of Control 91 (11), 2535–2548.
[5] Cieslak, J., Efimov, D., Henry, D., 2015. Transient management of a supervisory fault tolerant control scheme based on dwell-time conditions. International Journal of Adaptive Control and Signal Processing 29 (1), 123–142.
[6] Clifford, W. K., 1882. Mathematical papers. Macmillan and Company.

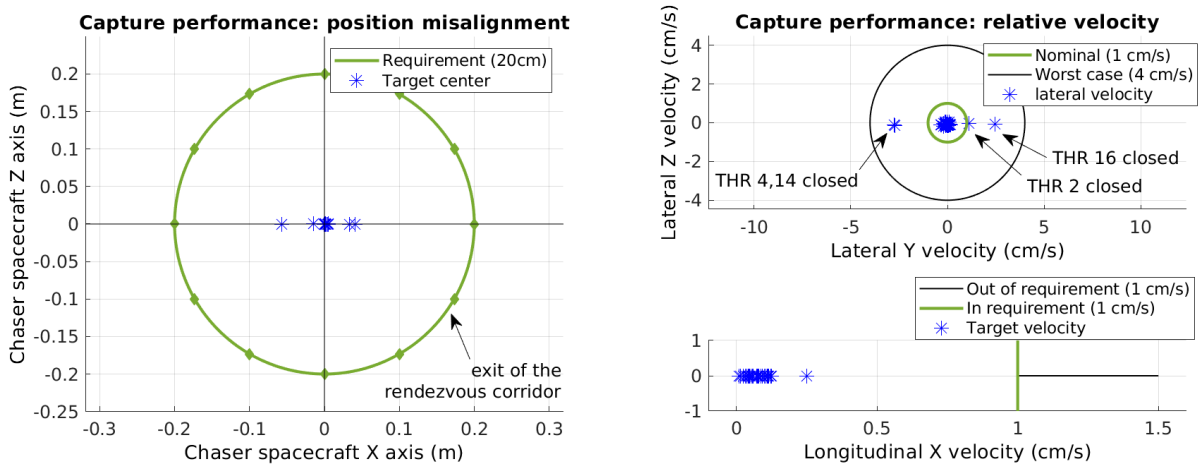

Figure 15: Simulation campaign with the FES (48 faulty cases - faults occur at $t = 40s$): a) position misalignment and b) relative velocities at the capture point

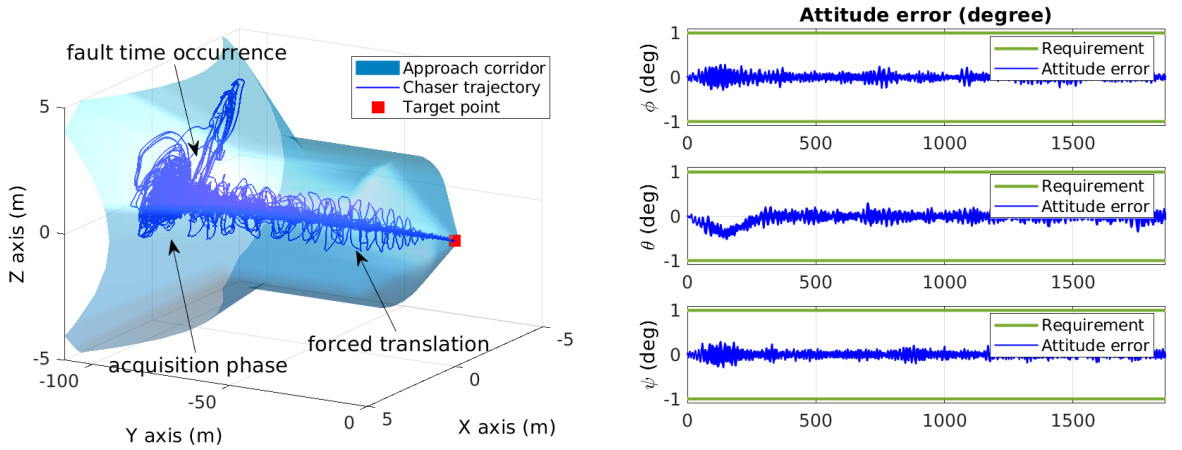

Figure 16: Simulation campaign with the FES (48 faulty cases - faults occur at $t = 40s$): a) chaser's position in the rendezvous corridor - b) attitude error

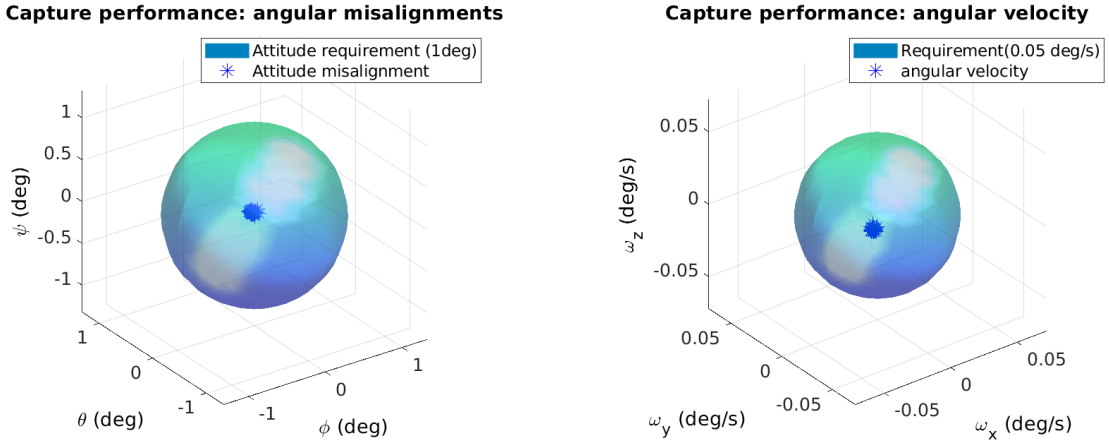

Figure 17: Simulation campaign with the FES (48 faulty cases - faults occur at $t = 40s$): a) attitude and b) angular velocity at the capture point.

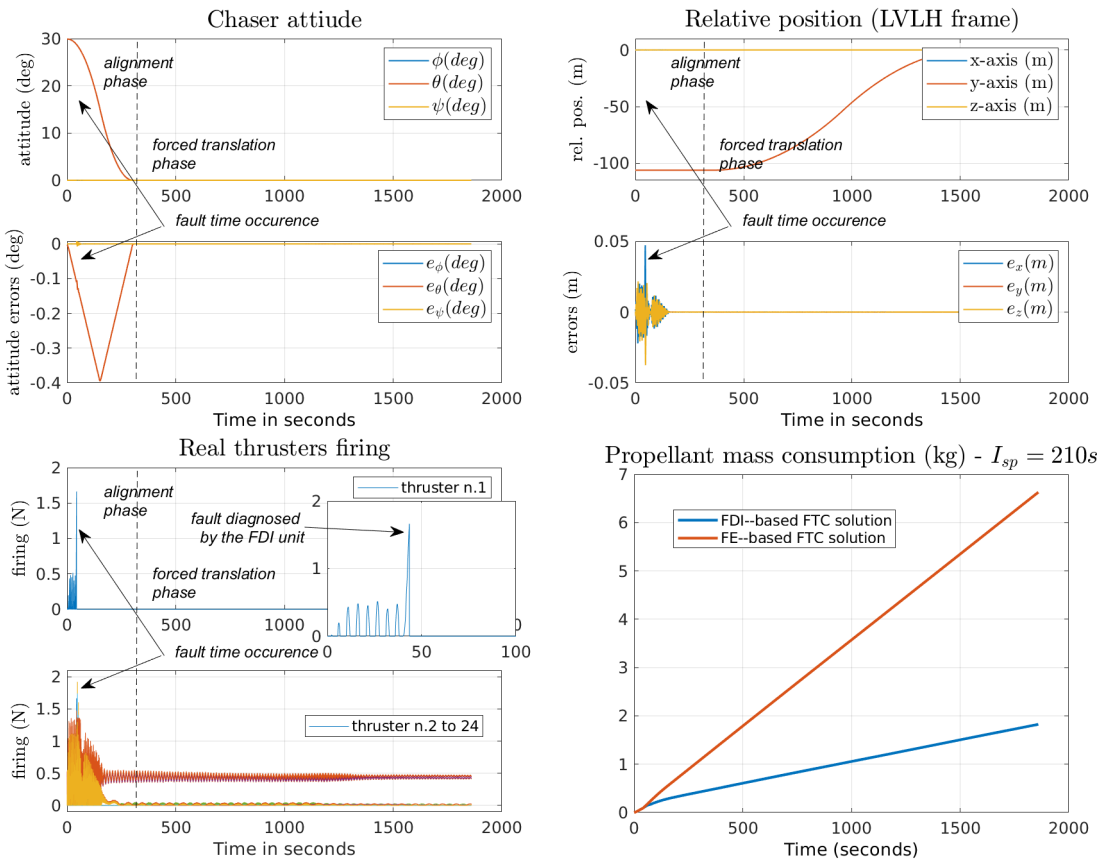

Figure 18: Perfect navigation and stuck-open fault in THR 1. FDI–based FTC solution : a) Attitude of the chaser - b) Relative position - c) real thruster's firing - d) Propellant consumption.

[7] Colmenarejo, P., Branco, J., Santos, N., Arroz, P., Telaar, J., Strauch, H., Ott, C., Reiner, M., Henry, D., Jaworski, J., Papadopoulos, E., Visentin, G., Ankersen, F., Gil-Fernandez, J., 2018. Methods and outcomes of the COMRADE project - design of robust coupled control for robotic spacecraft in servicing missions: trade-off between H_∞ and nonlinear lyapunov-based approaches. In: International Astronautical Congress. Bremen. Germany.

[8] Colmenarejo, P., Briz, J., Alcalde, A., Peters, T., Dubanchet, V., Henry, D., Menon, P., Ankersen, F., 2018. Advanced GNC for In-Orbit autonomous Assembly of flexible vehicles – IOA-GNC. In: International Astronautical Congress. Bremen. Germany.

[9] Colmenarejo, P., LePeuvédic, C., Guiotto, A., 2008. HARVD Development, Verification and Validation approach (from traditional GNC design/V&V framework simulator to real-time dynamic testing). In: ESA 7th GNC Conference. Tralee - Ireland.

[10] Colmenarejo, P., Santos, N., Telaarc, J., Ott, C., Henry, D., Visentin, G., 2020. Results of the COMRADE project: Combined control for robotic spacecraft and manipulator in servicing missions: Active debris removal and re-fuelling. In: 11th International ESA Conference on Guidance, Navigation & Control Systems. Sopot, Poland.

[11] Crosby, N., 2009. Solar extreme events 2005–2006: Effects on near-earth space systems and interplanetary systems. Advances in Space Research 43 (4), 559–564.

[12] Daniilidis, K., 1999. Hand-eye calibration using dual quaternions. The International Journal of Robotics Research 18 (3), 286–298.

[13] Ding, S., 2008. Model-based Fault Diagnosis Techniques - Design schemes, Algorithms and Tools. Springer-Verlag, Berlin Heidelberg.

[14] Ding, S., 2020. Advanced Methods for Fault Diagnosis and Fault-tolerant Control. Springer.

[15] Dong, H., Hu, Q., Friswell, M. I., Ma, G., 2017. Dual-quaternion-based fault-tolerant control for spacecraft tracking with finite-time convergence. IEEE Transactions on Control Systems Technology 25 (4), 1231–1242.

[16] Dong, H., Hu, Q., Ma, G., 2016. Dual-quaternion based fault-tolerant control for spacecraft formation flying with finite-time convergence. ISA transactions 61, 87–94.

[17] Dooley, J. R., McCarthy, J. M., April 1991. Spatial rigid body dynamics using dual quaternion components. In: Proceedings. 1991 IEEE International Conference on Robotics and Automation. pp. 90–95 vol.1.

[18] Efimov, D., Cieslak, J., Henry, D., 2013. Supervisory fault tolerant control with mutual performance optimization. International Journal of Adaptive Control and Signal Processing 27, 251–279.

[19] Filipe, N., Tsiotras, P., June 2013. Simultaneous position and attitude control without linear and angular velocity feedback using dual quaternions. In: 2013 American Control Conference. pp. 4808–4813.

[20] Filipe, N., Tsiotras, P., 2015. Adaptive position and attitude-tracking controller for satellite proximity operations using dual quaternions. Journal of Guidance, Control, and Dynamics 38 (4), 566–577.

[21] Filippov, A., 1988. Differential Equations with Discontinuos Right-hand Sides. Kluwer Academic Publishers, Dordrecht, The Netherlands.

[22] Fonod, R., Henry, D., Charbonnel, C., Bornschlegl, E., Losa, D., Bennani, S., 2015. Robust FDI for fault-tolerant thrust allocation with application to spacecraft rendezvous. Control Engineering Practice 42, 12–27.

[23] Gao, S., Jing, Y., Liu, X., Zhang, S., 2020. Finite-time attitude-tracking control for rigid spacecraft with actuator failures and saturation constraints. International Journal of Robust and Nonlinear Control 30 (5), 1903–1937.

[24] Gao, X., Teo, K. L., Duan, G.-R., 2012. Robust H_∞ control of spacecraft rendezvous on elliptical orbit. Journal of the Franklin Institute 349 (8), 2515–2529.

[25] Gao, Z., Zhou, Z., Qian, M., Lin, J., 2018. Active fault tolerant control scheme for satellite attitude system subject to actuator time-varying faults. IET Control Apilication 12 (3), 405–412.

[26] GMV Space, Thales Alenia Space, Swedish Space Corporation, SENER, Jenaoptronik, INTA, 2011. HARVD High Accuracy RendezVous Demonstrator - Final Presentation. 2.12.2011.

[27] Golestani, M., Esmaeilzadeh, S. M., Xiao, B., 2020. Fault-tolerant attitude control for flexible spacecraft subject to input and state constraint. Transactions of the Institute of Measurement and Control 42 (14), 2660–2674.

[28] Gui, H., de Ruiter, A. H., 2017. Adaptive fault-tolerant spacecraft pose tracking with control allocation. IEEE Transactions on Control Systems Technology (99), 1–16.

[29] Gui, H., Vukovich, G., 2017. Adaptive fault-tolerant spacecraft attitude control using a novel integral terminal sliding mode. International Journal of Robust and Nonlinear Control 27 (16), 3174–3196.

[30] Hamilton, W. R., 1848. Xi. on quaternions; or on a new system of imaginaries in algebra. The London, Edinburgh, and Dublin Philosophical Magazine and Journal of Science 33 (219), 58–60.

[31] Han, D., Wei, Q., Li, Z., Sun, W., 2008. Control of oriented mechanical systems: A method based on dual quaternion. Vol. 41. pp. 3836–3841, 17th IFAC World Congress.

[32] Han, Z., Zhang, K., Yang, T., 2016. Spacecraft attitude control using nonsingular finite-time convergence terminal sliding mode. In: 2016 IEEE Chinese Guidance, Navigation and Control Conference (CGNCC). pp. 618–623.

[33] Henry, D., 2008. Fault diagnosis of the MICROSCOPE satellite actuators using H_∞/H_- filters. AIAA Journal of Guidance, Control, and Dynamics 31 (3), 699–711.

[34] Henry, D., Ankersen, F., Strippoli, L., 2019. Chapter 9 - a class of unknown input observers under H_∞ performance for fault diagnosis: Application to the Mars Sample Return mission. In: Boubaker, O., Zhu, Q., Mahmoud, M. S., Ragot, J., Karimi, H. R., Dávila, J. (Eds.), New Trends in Observer-based Control. Emerging Methodologies and Applications in Modelling. Academic Press, pp. 225 – 266.

[35] Henry, D., Cieslak, J., Torres, J. Z., Colmenarejo, P., Branco, J., Santos, N., Serra, P., Telaard, J., Strauch, H., Giordano, A., Stefano, M., Ott, C., Reiner, M., Jaworski, J., Papadopoulos, E., Visentin, G., Ankersen, F., Fernandez, J., 2019. Model-based fault diagnosis and tolerant control: the ESA's e.Deorbit mission. In: European Control Conference. Naples, Italy, pp. 4356–4361.

[36] Henry, D., Le Peuvédic, C., Strippoli, L., Ankersen, F., 2015. Robust model-based fault diagnosis of thruster faults in spacecraft. IFAC-PapersOnLine - SAFEPROCESS'2015 48 (21), 1078–1083.

[37] Henry, D., Le Peuvédic, C., Strippoli, L., Ankersen, F., 2016. Model-based FDIR and fault accommodation for a rendezvous mission around the Mars planet: the Mars Sample Return case. IFAC-PapersOnLine 49 (5), 266–271.

[38] Herrmann, G., Menon, P. P., Turner, M. C., Bates, D. G., Postlethwaite, I., 2010. Anti-windup synthesis for nonlinear dynamic inversion control schemes. International Journal of Robust and Nonlinear Control 20 (13), 1465–1482.

[39] Hu, H., Liu, L., Wang, Y., Cheng, Z., Luo, Q., 2020. Active fault-tolerant attitude tracking control with adaptive gain for spacecrafts. Aerospace Science and Technology 98, 105706.

[40] Hu, Q., Niu, G., Wang, C., 2018. Spacecraft attitude fault-tolerant control based on iterative learning observer and control allocation. Aerospace Science and Technology 75, 245–253.

[41] Hu, Q., Shao, X., 2016. Smooth finite-time fault-tolerant attitude tracking control for rigid spacecraft. Aerospace Science and Technology 55, 144–157.

[42] Huijun, G., Xuebo, Y., Shi, P., 2009. Multi-objective robust H_∞ control of spacecraft rendezvous. IEEE Transactions on Control Systems Technology 17 (4), 794–802.

[43] Hutton, J. M., 2020. A Closer Look at Fault-tolerant Control. Nova Science Publishers, Inc. ISBN: 978-1-53617-528-8.

[44] Jewison, C. M., 2017. Guidance and control for multi-stage rendezvous and docking operations in the presence of uncertainty. Massachusetts Institute of Technology.

[45] Jiang, B., Hu, Q., Friswell, M. I., 2016. Fixed-time attitude control for rigid spacecraft with actuator saturation and faults. IEEE Transactions on Control Systems Technology 24 (5), 1892–1898.

[46] Jiang, B., Hu, Q., Friswell, M. I., 2016. Fixed-time rendezvous control of spacecraft with a tumbling target under loss of actuator effectiveness. IEEE Transactions on Aerospace and Electronic Systems 52 (4), 1576–1586.

[47] Jin, H., Wiktor, P., DeBra, D., 1995. An optimal thruster configuration design and evaluation for quick step. Control Engineering Practice 3 (8), 1113–1118.

[48] Jing, C., Xu, H., Niu, X., Song, X., 2019. Adaptive nonsingular terminal sliding mode control for attitude tracking of spacecraft with actuator faults. IEEE Access 7, 31485–31493.

[49] Jüttler, B., 1994. Visualization of moving objects using dual quaternion

curves. Computers & Graphics 18 (3), 315–326.
[50] Kenwright, B., 2012. A beginners guide to dual-quaternions: What they are, how they work, and how to use them for 3d character hierarchies. In: The 20th International Conference in Central Europe on Computer Graphics, Visualization and Computer Vision. Plzen, Czech Republic, pp. 1–10.
[51] Kristiansen, R., Nicklasson, P. J., Gravdahl, J. T., 2008. Spacecraft coordination control in 6DOF: Integrator backstepping vs passivity-based control. Automatica 44 (11), 2896–2901.
[52] Lan, J., Patton, R. J., 2018. A decoupling approach to integrated fault-tolerant control for linear systems with unmatched non-differentiable faults. Automatica 89, 290 – 299.
[53] Lee, D., Sanyal, A. K., Butcher, E. A., 2014. Asymptotic tracking control for spacecraft formation flying with decentralized collision avoidance. Journal of Guidance, Control, and Dynamics 38 (4), 587–600.
[54] LePeuvédic, C., Colmenarejo, P., A.Guiotto, 2008. Autonomous rendezvous control system: a high fidelity functional engineering simulator for GNC/AMM/FDIR validation. In: ESA 7th GNC Conference. Tralee - Ireland.
[55] Li, B., Hu, Q., Yang, Y., 2019. Continuous finite-time extended state observer based fault tolerant control for attitude stabilization. Aerospace Science and Technology 84, 204–213.
[56] Li, B., Hu, Q., Yu, Y., Ma, G., 2017. Observer-based fault-tolerant attitude control for rigid spacecraft. IEEE Transactions on Aerospace and Electronic Systems 53 (5), 2572–2582.
[57] Lu, K., Xia, Y., 2013. Finite-time fault-tolerant control for rigid spacecraft with actuator saturations. IET Control Theo Appl 11 (7), 1529–1539.
[58] Lu, K., Xia, Y., Fu, M., Yu, C., 2016. Adaptive finite-time attitude stabilization for rigid spacecraft with actuator faults and saturation constraints. International Journal of Robust and Nonlinear Control 26 (1), 28–46.
[59] Lv, Y., Hu, Q., Ma, G., Zhou, J., 2011. 6 DOF synchronized control for spacecraft formation flying with input constraint and parameter uncertainties. ISA transactions 50 (4), 573–580.
[60] Montenbruck, O., Gill, E., 2012. Satellite Orbits. Models, Methods, Applications (4th Ed.). Springer.
[61] Moreno, J. A., 2009. A linear framework for the robust stability analysis of a generalized super-twisting algorithm. In: 2009 6th International Conference on Electrical Engineering, Computing Science and Automatic Control (CCE). pp. 1–6.
[62] NASA, 2007. Lewis spins out of control. System Failure Case Studies 1 (8), 1–4.
[63] Patton, R., Frank, P., Clark, R., 2000. Issues of fault diagnosis for dynamic systems. Springer, London, ISBN 3-540-19968-3.
[64] Patton, R. J., Lan, J., 2020. Robust Integration of Model-Based Fault Estimation and Fault-Tolerant Control. Springer International Publishing. ISBN: 978-3-030-58759-8.
[65] Pittet, C., Falcoz, A., Henry, D., 2016. A model-based diagnosis method for transient and multiple faults of aocs thrusters. In: 20th IFAC Symposium on Automatic Control in Aerospace ACA 2016. Vol. 49. IFAC, Sherbrooke, Quebec, Canada, pp. 82–87.
[66] Qian, M., Shi, Y., Gao, Z., Zhang, X., 2020. Integrated fault tolerant tracking control for rigid spacecraft using fractional order sliding mode technique. Journal of the Franklin Institute 357 (15), 10557 – 10583.
[67] Robertson, B., Stoneking, E., 2003. Satellite GN&C anomaly trends. Advances in the Astronautical Sciences 113, 531–542.
[68] Shahna, M. H., Abedi, M., 2020. An anti-unwinding finite time fault tolerant sliding mode control of a satellite based on accurate estimation of inertia moments. ISA Transactions 101, 23 – 41.
[69] Sharma, R., Sengupta, P., Srinivas, R., 2007. Near-optimal feedback rendezvous in elliptic orbits accounting for nonlinear differential gravity. Journal of Guidance, Control, and Dynamics 30 (6), 1803–1813.
[70] Shen, Q., Jiang, B., Shi, P., 2017. Fault Diagnosis and Fault-Tolerant Control Based on Adaptive Control Approach. Springer.
[71] Shen, Q., Wang, D., Zhu, S., Poh, E. K., 2015. Integral-type sliding mode fault-tolerant control for attitude stabilization of spacecraft. IEEE Transactions on Control Systems Technology 23 (3), 1131–1138.
[72] Shen, Q., Wang, D., Zhu, S., Poh, K., 2015. Finite-time fault-tolerant attitude stabilization for spacecraft with actuator saturation. IEEE Transactions on Aerospace and Electronic Systems 51 (3), 2390–2405.
[73] Shibata, M., Ichikawa, A., 2007. Orbital rendezvous and flyaround based on null controllability with vanishing energy. Journal of Guidance, Control, and Dynamics 30 (4), 934–945.
[74] Shtessel, Y., Edwards, C., Fridman, L., Levant, A., 2015. Sliding Mode Control and Observation, 1st Edition. Birkhauser Basel.
[75] Sidi, M. J., 1997. Spacecraft dynamics and control: a practical engineering approach. Vol. 7. Cambridge university press.
[76] Soderlund, A., Phillips, S., Zaman, A., Petersen, C., 2021. Autonomous satellite rendezvous and proximity operations via geometric control methods. In: AIAA Scitech 2021 Forum. pp. 1–13.
[77] Sun, L., Huo, W., 2015. Robust adaptive relative position tracking and attitude synchronization for spacecraft rendezvous. Aerospace Science and Technology 41, 28–35.
[78] Syfert, M., Sztyber, A., Koscielny, J., 2017. Advanced Solutions in Diagnostics and Fault Tolerant Control. Springer.
[79] Tafazoli, M., 2009. A study of on-orbit spacecraft failures. Acta Astronautica 64 (2), 195–205.
[80] Torres, J. Z., Cieslak, J., Henry, D., Dávila, J., 2019. A super-twisting sliding mode control in a backstepping setup for rendezvous with a passive target. IFAC-PapersOnLine 52 (12), 25 – 30, 21st IFAC Symposium on Automatic Control in Aerospace ACA 2019.
[81] Varga, A., 2017. Solving Fault Diagnosis Problems: Linear Synthesis Techniques. Vol. 84 - ISBN : 978-3-319-51558-8. Springer.
[82] Walker, M. W., Shao, L., Volz, R. A., 1991. Estimating 3-d location parameters using dual number quaternions. CVGIP: image understanding 54 (3), 358–367.
[83] Wang, J., Liang, H., Sun, Z., Zhang, S., Liu, M., 2012. Finite-time control for spacecraft formation with dual-number-based description. Journal of Guidance, Control, and Dynamics 35 (3), 950–962.
[84] Wang, J., Sun, Z., 2012. 6-DOF robust adaptive terminal sliding mode control for spacecraft formation flying. Acta Astronautica 73, 76–87.
[85] Wang, J.-Y., Liang, H.-Z., Sun, Z.-W., Wu, S.-N., Zhang, S.-J., 2013. Relative motion coupled control based on dual quaternion. Aerospace Science and Technology 25 (1), 102–113.
[86] Wang, X., Yu, C., 2010. Feedback linearization regulator with coupled attitude and translation dynamics based on unit dual quaternion. In: 2010 IEEE International Symposium on Intelligent Control, Part of 2010 IEEE Multi-Conference on Systems and Control. IEEE, Yohohama,Japan, p. 2380–238.
[87] Wied, B., 1998. Space vehicle dynamics and control. Reston, VA: American Institute of Aeronautics and Astronautics.
[88] Wu, Y., Hu, X., Hu, D., Li, T., Lian, J., 2005. Strapdown inertial navigation system algorithms based on dual quaternions. IEEE Transactions on Aerospace and Electronic systems 41 (1), 110–132.
[89] Xiao, B., Hu, Q., Zhang, Y., 2012. Adaptive sliding mode fault tolerant attitude tracking control for flexible spacecraft under actuator saturation. IEEE Transactions on Control Systems Technology 20 (6), 1605–1612.
[90] Yang, X., Yu, J., Gao, H., 2012. An impulse control approach to spacecraft autonomous rendezvous based on genetic algorithms. Neurocomputing 77 (1), 189–196.
[91] Zenteno-Torres, J., Cieslak, J., Dávila, J., Henry, D., 2021. Sliding mode control with application to fault-tolerant control: Assessment and open problems. Automation 2 (1), 1–30.
[92] Zenteno-Torres, J., Cieslak, J., Henry, D., Dávila, J., 2017. Fault compensability criteria with application to a rendezvous mission around Mars. In: 2017 14th European Workshop on Advanced Control and Diagnosis (ACD). Buccharest, Romania.
[93] Zenteno-Torres, J., Cieslak, J., Henry, D., Dávila, J., 2018. A tracking backstepping sliding-mode control for spacecraft rendezvous with a passive target. In: 2018 UKACC 12th International Conference on Control (CONTROL). pp. 69–74.
[94] Zenteno-Torres, J., Cieslak, J., Henry, D., Dávila, J., 2019. A sliding mode control in a backstepping setup for rendezvous mission on a circular orbit. In: 8th European Conference for Aeronautics and Space Sciences. Madrid, Spain.
[95] Zhang, C., Wang, J., Zhang, D., Shao, X., 2018. Fault-tolerant adaptive finite-time attitude synchronization and tracking control for multi-spacecraft formation. Aerospace Science and Technology 73, 197–209.
[96] Zhou, B., Lin, Z., Duan, G.-R., 2011. Lyapunov differential equation approach to elliptical orbital rendezvous with constrained controls. Journal of Guidance, Control, and Dynamics 34 (2), 345–358.